





## RESEARCH ARTICLE

10.1029/2022EA002278

# DeepLandforms: A Deep Learning Computer Vision Toolset Applied to a Prime Use Case for Mapping Planetary Skylights

Giacomo Nodjoui<sup>1</sup> , Riccardo Pozzobon<sup>2,3</sup>, Francesco Sauro<sup>4</sup>, and Angelo Pio Rossi<sup>1</sup> 

### Special Section:

Exploring planetary caves as windows into subsurface geology, habitability, and astrobiology

<sup>1</sup>Constructor University Bremen gGmbH (formerly Jacobs University Bremen), Bremen, Germany, <sup>2</sup>INAF-Astronomical Observatory of Padova, Padova, Italy, <sup>3</sup>Department of Geosciences, University of Padova, Padova, Italy, <sup>4</sup>Department of Biological, Geological and Environmental Sciences, University of Bologna, Bologna, Italy

### Key Points:

- Instance Segmentation methodology is used to map landforms obtaining vectorial data in geopackage file format
- A newly developed composite toolset to perform image pre-processing, data labeling, model training and inference tasks is presented
- The results of a prime case of mapping pit and skylights on Mars surface are showed

### Supporting Information:

Supporting Information may be found in the online version of this article.

### Correspondence to:

G. Nodjoui,  
g.nodjoui@jacobs-university.de

### Citation:

Nodjoui, G., Pozzobon, R., Sauro, F., & Rossi, A. P. (2023). DeepLandforms: A Deep Learning computer vision toolset applied to a prime use case for mapping planetary skylights. *Earth and Space Science*, 10, e2022EA002278. <https://doi.org/10.1029/2022EA002278>

Received 9 FEB 2022  
Accepted 15 DEC 2022

### Author Contributions:

**Conceptualization:** Giacomo Nodjoui, Riccardo Pozzobon, Francesco Sauro, Angelo Pio Rossi

**Data curation:** Giacomo Nodjoui

**Formal analysis:** Giacomo Nodjoui

**Funding acquisition:** Angelo Pio Rossi

**Abstract** Thematic map creation is a meticulous process that requires several steps to be accomplished regardless of the type of map to be produced, from data collection, through data exploitation and map publication in print, image, and GIS format. Examples are geolithological, and geomorphological maps in which most of the highest time-consuming tasks are those related to the discretization of single objects. Introducing also interpretative biases because of the different experience of the mappers in identifying a set of unique characteristics that describe those objects. In this setting, Deep Learning Computer Vision techniques could play a key role but lack the availability of a complete set of tools specific for planetary mapping. The aim of this work is to develop a comprehensive set of ready-to-use tools for landforms mapping based on validated Deep Learning methodologies and open-source libraries. We present *DeepLandforms*, the first pre-release of a toolset for landform mapping using Deep Learning that includes all the components for data set preparation, model training, monitoring, and inference. In *DeepLandforms*, users have full access to the workflow and control over all the processes involved, granting complete control and customization capabilities. In order to validate the applicability of our tool, in this work we present the results achieved using *DeepLandforms* in the science case of mapping sinkhole-like landforms on Mars, as a first example that can lead us into multiple and diverse future applications.

**Plain Language Summary** The creation of maps is a complex set of several tasks that, regardless of the type of map, are often very time-consuming. For instance, all the occurrences of a specific object, natural or man-made in a defined area, need to be identified, drawn and classified manually. Mapping large objects in small areas is an easy task but may be unmanageable in cases such as small landforms on the entire surface of a planet. Nowadays, especially on Earth, researchers and professionals take advantages of highly specialized software based on a technique called Deep Learning. Such software are almost never free nor ready-to-use and often requires higher knowledge in computer programming languages. In this work, we present the first pre-release of a novel open-source computer software, nearly ready-to-use, that provides all the instruments for approaching Deep Learning for automatic landforms mapping. We present also the results obtained by trying this software using data of Mars's surface to map sinkhole-like landforms.

## 1. Introduction

The exploration of terrestrial planets in the Solar System was and still is performed mainly on data that cover almost all the electromagnetic spectrum, acquired over the last century by several types of orbiters, rovers, and landers. Planetary data volumes are constantly increasing both in quality and quantity, with the contribution of both public and private entities.

Imagery has always been the primary resource for researchers in planetary sciences, especially for geologists and geomorphologists. In the last two decades, the progress in the development of very high-resolution image sensors gave the community access to images with a spatial resolution on the order of centimeters. Data collected by High Resolution Imaging Science Experiment (HiRISE) instrument, on board of the Mars Reconnaissance Orbiter (MRO) (McEwen et al., 2007) or by the Narrow Angle Camera experiment, on board of Lunar Reconnaissance Orbiter (Robinson et al., 2010), have been used in several works to constrain the surface properties of respectively, Mars and the Moon.

For instance, several publications investigate specific surface features morphometry, such as impact of megabreccia (Grant et al., 2008), crater counting (Benedix et al., 2020; Chen et al., 2017; Robbins & Hynek, 2014;

© 2022 The Authors. Earth and Space Science published by Wiley Periodicals LLC on behalf of American Geophysical Union.

This is an open access article under the terms of the [Creative Commons Attribution License](https://creativecommons.org/licenses/by/4.0/), which permits use, distribution and reproduction in any medium, provided the original work is properly cited.

**Investigation:** Giacomo Nodjoumi  
**Methodology:** Giacomo Nodjoumi  
**Resources:** Angelo Pio Rossi  
**Software:** Giacomo Nodjoumi  
**Supervision:** Angelo Pio Rossi  
**Validation:** Giacomo Nodjoumi, Riccardo Pozzobon, Angelo Pio Rossi  
**Writing – original draft:** Giacomo Nodjoumi  
**Writing – review & editing:** Giacomo Nodjoumi, Riccardo Pozzobon, Francesco Sauro, Angelo Pio Rossi

Servis et al., 2020; Watters et al., 2015), or boulder counting (Le Mouélic et al., 2020; Sargeant et al., 2020; Watkins et al., 2017). Other publications are focused on the characterization of polar layered deposits (Milkovich et al., 2009) and identification of the source of ice blocks in the north polar cap (Su et al., 2021). Others, not only investigate morphological properties but also perform comparative analyses and numerical modeling (Guimpier et al., 2021), or in-depth analyses of Mars's surface processes (Guallini et al., 2018; Luzzi et al., 2020). These surface processes include skylight, pits (Barlow et al., 2017; Cushing, 2017; Cushing et al., 2015; Haruyama et al., 2009; Michikami et al., 2014; Sharma & Srivastava, 2021; Wagner & Robinson, 2014; Wyrick, 2004; Xiao et al., 2014), and pit chains (Wyrick, 2004). Further works involve the application of advanced techniques, such as Structure-from-Motion, (Le Mouélic et al., 2020; Micheletti et al., 2015; Muller et al., 2021; Y. Wang et al., 2021), Shape-from-Shading (SfS) (Alexandrov & Beyer, 2018; Lohse et al., 2006) and Machine Learning for object detection and classification (Barrett et al., 2022; Dunder et al., 2019; Hipperson et al., 2020; Hu et al., 2021; Lee, 2019; Nodjoumi et al., 2021; Palafox et al., 2017; Rashno et al., 2017; Silburt et al., 2019; Wilhelm et al., 2020).

This leap in image quality and quantity has introduced new challenges for researchers since the higher resolutions brought the great advantage of being able to analyze the surface of those planets with unprecedented detail.

Nevertheless, the computational power requirements to process such bigger data have also increased, especially when performing large-scale feature mapping.

Teams and groups of researchers specialized in single to multiple fields aim to combine their knowledge to describe and characterize the surface of a planet, but producing a map requires carrying out multiple and complex tasks (Geomorphological Mapping, 2013; Napieralski et al., 2013; Nass et al., 2021). Depending on the type of map in production, these tasks may vary but at least four major focal tasks are shared across all map types: (a) data collection, (b) data exploitation, (c) map creation, and (d) map dissemination (Naß et al., 2017, 2021). Among those major tasks, the most time-consuming sub-tasks are the definition of the standards for map production and dissemination (Hare et al., 2018) and the proper digital creation of map elements by manually drawing all the features of the area of interest using a GIS software. For instance, in geomorphological mapping, the primary target is the identification of landforms. The term landform is defined as a topographic expression on the surface of a planetary body that can be described by at least seven parameters: shape, size, height, texture, pattern, tone/hue, location/association (Tempfli et al., 2009). Multiple landforms in an area constitute a terrain (Bridge & Demicco, 2008; DiPietro, 2013); for further details, we refer the reader to Table S1 in Supporting Information S1.

The formation mechanisms of landforms and terrains complexly combine interconnected settings, processes, and forces, some of which are more wide and planetary-scale dependent, while others are more related to specific environmental and atmospheric characteristics.

For instance, the size and shape of different morphologies, such as lava tubes and rilles on the Moon, Mars, and Earth, (Bardabelias et al., 2020; Chappaz et al., 2017; Cruikshank & Wood, 1972; Greeley, 1971; Haruyama et al., 2009; Horvath et al., 2020; Kaku et al., 2017; Léveillé & Datta, 2010; F. Sauro et al., 2020; Whitten & Martin, 2019) depends not only on the geological settings of the area but also on the gravity intensity.

Similarly to lava tubes morphologies, landslides (Hungr et al., 2014) and sinkholes (Parise, 2019) formation and driving mechanisms are deeply interconnected to gravity, geological settings, and atmospheric characteristics. These landforms are found both on Mars (Bardabelias et al., 2020; Cushing et al., 2007; De Blasio, 2011; Guimpier et al., 2021; Hooper & Smart, 2013; Sharma & Srivastava, 2021), as well as on Earth (Acharya et al., 2006; Díaz Michelena et al., 2020; Gutiérrez et al., 2008; Hungr et al., 2014; Jiang, 2020; Parise, 2019; Van Den Eeckhaut et al., 2007; Youssef et al., 2012) thus may have common formation mechanisms.

Conversely, several authors found correlations between the presence of liquid-water seasonal precipitation, groundwater circulation and the occurrence of landslides and sinkholes. On Earth, the presence of liquid water is not only a driving mechanism but also a trigger for many geological and geomorphological processes (Allemant et al., 2011; Alonso et al., 2010; Cahalan & Milewski, 2018; Díaz Michelena et al., 2020; Duhart et al., 2019; Gutiérrez et al., 2008; Jiang, 2020; Lacerda et al., 2004; Lin et al., 2004; Van Den Eeckhaut et al., 2007; Youssef et al., 2012), while it is still under debate on those similar processes found on Mars and other rocky planets (De Blasio, 2011; Guimpier et al., 2021; Hooper & Smart, 2013; Salese et al., 2019; Smith et al., 2006).

Several types of terrains and thus landforms are peculiar to specific areas or even planets or moons. For instance, Chaotic Terrains are planetary surface features notably found on Mars, Mercury, Jupiter's moon Europa and Pluto (Luzzi et al., 2020, 2021; Skjetne et al., 2021). Mountains, hills, plains volcanoes are common in almost all rocky planets of the Solar System (Hargitai & Kereszturi, 2015).

The occurrence of specific landforms is deeply connected to the geology of the area, the past and present atmospheric processes. Besides natural processes, anthropological activities have a great impact on the shaping of the landscape. This is valid not only on Earth but also to a certain extent, to robotic or human landing sites.

(Brierley et al., 2021; James et al., 2013; Slaymaker et al., 2021). Studying those features is essential to better know the relations between the main processes involved in the characterization and evolution of an area.

Identification, classification, and description of landforms are done by mappers using multiple data types and sources such as images in various spectra, previous maps, digital terrain models (DTMs) and so on (Luzzi et al., 2020; Parente et al., 2019; Sivakumar et al., 2017). The time necessary to accomplish this specific sub-task strictly depends on the scale of the area of interest and the scale of the features within, since wider areas and smaller features may lead to extremely high workloads. The final map product is a fundamental element to consider while estimating the complexity of map production work. This is due to the wide diversity of map products available, and thus to the parameters to be defined and the data to be collected and processed.

Geological maps consider spatial-temporal relations between surface and subsurface's features, their compositions and the past and present geological processes involved (Martinot et al., 2018; Naß & van Gasselt, 2021; Pondrelli et al., 2020; Sun & Stack, 2020; Tsubulskaya et al., 2020). Undoubtedly, visual properties derived from images like colors, texture, patterns, etc., take an essential role in the area's analysis (Kumar et al., 2019; Tirsch et al., 2021; Tsubulskaya et al., 2020; B. Wu et al., 2020).

In addition, the data collection steps can be very time-consuming tasks, beyond being also complex, since most of the data needs to be pre-processed prior to the proper analysis. For example, there are over 1.8 million products of HiRISE acquisitions that are over 49 Terabyte for a single imager that is still acquiring data at the time of writing.

In this framework, Deep Learning computer vision methodologies are robust and widely accepted and applied both on Earth for crops monitoring and management (Grace et al., 2021), land use (Rousset et al., 2021; Talukdar et al., 2020), risk management and assessment (Ghorbanzadeh et al., 2019; Liu et al., 2004; Merghadi et al., 2020; Paul & Ganju, 2021; Tien Bui et al., 2016; Yousefi et al., 2020); and on other Solar System planetary body (Barrett et al., 2022; Dundar et al., 2019; Hipperson et al., 2020; Lee, 2019; Palafox et al., 2017; Rashno et al., 2017; Stepinski et al., 2007; S. Wang et al., 2020; Wilhelm et al., 2020); thus, these technologies may play a crucial role in exploiting such a large amount of data.

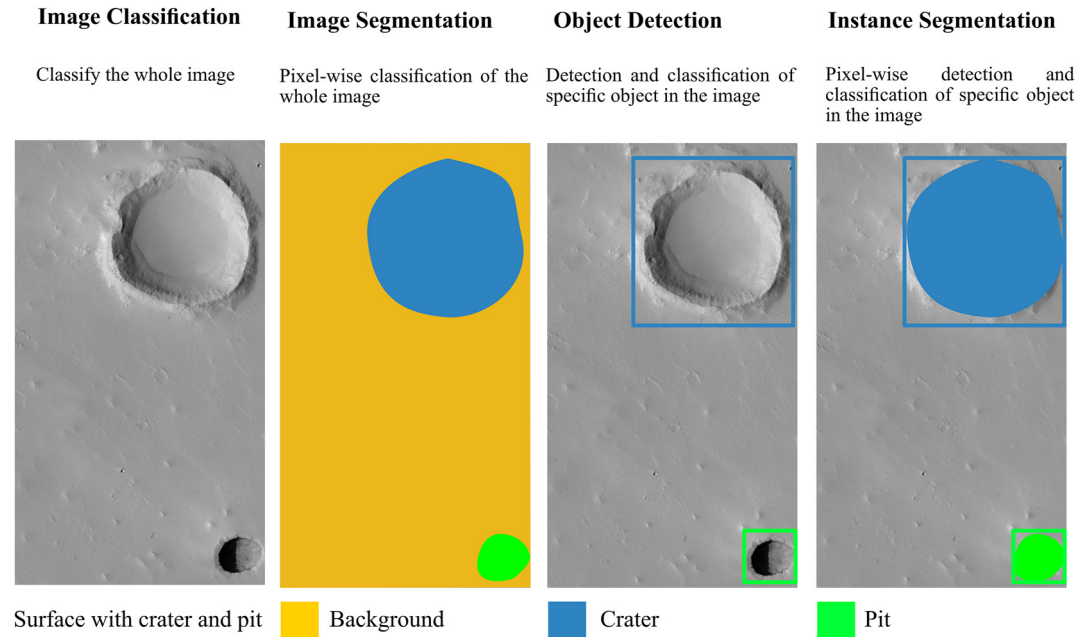
The objectives of these methodologies are mainly the four types listed below and shown in Figure 1.

The first method displayed in Figure 1 is *Image Recognition (ImR)* which classifies the whole image contents. The second, called *Image Segmentation (ImS)*, classifies each pixel of the image and creates segments of adjacent pixels with contiguous classification. The third technique, *Object Detection (OD)*, locates the objects using bounding boxes and classifies them separately, while the fourth, *Instance Segmentation (InS)* is a combination of the second and the third method, getting the segmentation of only the objects identified by the detection.

In brief, each method uses complex computer codes to train a neural network model on a data set that contains images and class labels for each target of interest. This training comprises a cyclical series of mathematical and statistical operations which extract the embedded and unique features that describe each class target.

Those architectures may require a tremendous amount of well-labeled training data in order to better generalize the model and avoid over-fitting and underfitting problems (Zhang et al., 2021). More detailed descriptions are available in Text S1 in Supporting Information S1.

Such training data are not always ready-to-use for labeling, mostly because of compatibility issues between labeling software, deep learning software and the data itself. Data size and file format are the main issues, and therefore pre-processing tasks have a key role and are mandatory for any approach, especially if geo-referencing information is required. We provide a more detailed overview in Text S3 in Supporting Information S1 along with the pre-processing steps.



**Figure 1.** Comparison between image recognition, image segmentation, object detection and instance segmentation for the specific case of geomorphology mapping.

Nowadays, Deep Learning methodologies are widely and commonly used to solve several daily problems. For instance, facial recognition features of social networks, Google images search, security surveillance and much more, but also specific problems relative to Earth Observation such as land coverage, crops vegetation monitoring, early warning systems and other (Brust et al., 2019; Hoerer & Kuenzer, 2020; Miyamoto et al., 2018; Redmon et al., 2016; Szegedy et al., 2013; Y. Wu et al., 2019, 2020; Zhao et al., 2019).

In the last two decades, many efforts have been made to use Deep Learning for the resolution of planetary mapping problems on Earth (Liu et al., 2004; Paul & Ganju, 2021; Stepinski et al., 2007; Talukdar et al., 2020) as well as on Mars (Hipperson et al., 2020; Nagle-McNaughton et al., 2020; Palafox et al., 2017; Wilhelm et al., 2020) and the Moon (Hu et al., 2021; Silburt et al., 2019; S. Wang et al., 2020) exploring almost all architectures and algorithms with very promising results.

Sometimes, the code used for the analysis is publicly available (Aye et al., 2019; Barrett et al., 2022; Lee, 2019; Silburt, 2017/2019; Wilhelm et al., 2020) and may be used to create preliminary map products.

The results obtained with the above-mentioned codes are typically plain images with the bounding boxes or the segmented area superimposed and are in non-geo-referenced raster file type formats, such as png or jpeg. Those type of results need to be georeferenced before being further processed in GIS software to manually vectorize all the objects or segments. For instance, segmented areas such as those that represent geomorphological units need to be manually digitized as individual shapes in GIS software, with the manual conversion and assignment of the properties of the units in the image.

Finally, after completing the digitation, mappers can obtain a vectorial map that can be published in a geospatial data format such as OGC Geopackage. This newer file format is specific for transferring geospatial information similarly to ESRI shapefiles (ESRI technical document, 1998), but with higher portability and compactness, and moreover it is an open format and standards-based (Open Geospatial Consortium, 2021).

Geologists and geomorphologists, who are not familiar with programming languages but are interested only in workflows and tools can find it difficult to understand and use complex machine learning approaches that require higher knowledge in computer science, especially if complete and ready-to-use tools are not available.

In this article, we present a first complete working release of *DeepLandforms*, a set of comprehensive and ready-to-use tools specifically developed for planetary mapping.

This toolset is a follow-up of the work reported in (Nodjoumi et al., 2021), based on the object detection methodology and focused on the usage of You Only Look Once version 5 (YOLOv5) framework (Pham et al., 2020; Ultralytics/Yolov5, 2020/2021) to detect sinkhole-like landforms on Mars, obtaining a geopackage containing the centroid coordinates of the bounding boxes, the confidence level, and the classification class for each of the detections. While centroid coordinates could be considered a starting point for proper mapping, there is a lack of spatial dimensionality, can provide only a general localization of the features, and even using the coordinates of the detection boxes we still lack a precise localization and definition of the shapes of the landforms. To further improve the previous work, a change of architecture was needed, moving from object detection to instance segmentation architecture.

The instance segmentation library selected for this work is the Detectron2 Library, developed and periodically maintained by the Facebook AI Research team, specialized in *ImS* tasks through R-CNN networks. See Text S2 in Supporting Information S1 for additional details on Detectron2 Library.

In this work, the Mask R-CNN network has been considered the only main network since it is specific for object instance segmentation tasks (He et al., 2018). Mask R-CNN extends Faster R-CNN, which produces only class labels and bounding boxes, by adding a third output, the object masks (He et al., 2018; Massa & Girshick, 2018). A mask can be considered as a method of describing an image in boolean-based representation by using specific filters or functions, meaning that the content of the image will be converted to only two possible values (0–1, on-off, true-false, and so on) (Text S4 and Figure S3 in Supporting Information S1). Each mask is then characterized by internal and external values and can be localized by using image pixel coordinates.

## 2. DeepLandforms

*DeepLandforms* has been developed with the aim of creating a comprehensive set of tools to support a complete workflow for mapping landforms using geo-referenced data and producing results in vectorial format. A flow-chart of the workflow is depicted in Figure 2 and is based on the general Deep Learning workflow summarized in Text S3 in Supporting Information S1.

Although the complete workflow contains data preparation and model training, it is possible to use all the components as a standalone tool. For instance, *DeepLandforms-Inference* component can be used to analyze geo-referenced images by passing a Detectron2 model trained elsewhere. The whole workflow is not bounded only to EDR/PDS data and so each component can work with any images as long as are geo-referenced and in GeoTiff/JPEG/PNG file format.

A detailed description of each step of the workflow is available in Section 3.2.

### 2.1. Components

The toolset is composed of four major components, all based on the Docker open platform (Docker overview, 2021; Merkel, 2014), a state-of-the-art, well-known, open-source platform for developing, sharing and running applications as sandbox services called *containers*, with full support for NVIDIA GPU (CUDA) computing (Luebke, 2008).

The major advantage of using Docker platform consists in the capabilities of running services in an instantiated environment, independent from the host operating system without worrying about library dependencies, compilers, interpreters and so on, thus providing great cross-platform compatibility. Docker containers can be shared both as pre-built container images for fast deployment and as a Docker building recipe named Dockerfile. Those recipes can be customized by combining with other dockerfiles and/or, with pre-build Docker images. Dockerfiles can also be used in combination with docker-compose (Merkel, 2014), a tool for running multi-container Docker applications.

The first component is the *ImageProcessingUtils* Docker container (Nodjoumi, 2021b), a Jupyter notebook tool developed for resizing, cropping, removing black borders, tiling and converting images from CUB (Anderson Jeff & Deborah Lee Soltesz, 2003), jpeg2000 and GeoTiff file formats to GeoTiff (including Cloud Optimized GeoTiff), jpeg and png file formats. This notebook processes the images while maintaining georeferencing information in the file metadata for GeoTiff or in ancillary files for jpeg and png formats. The second component is the



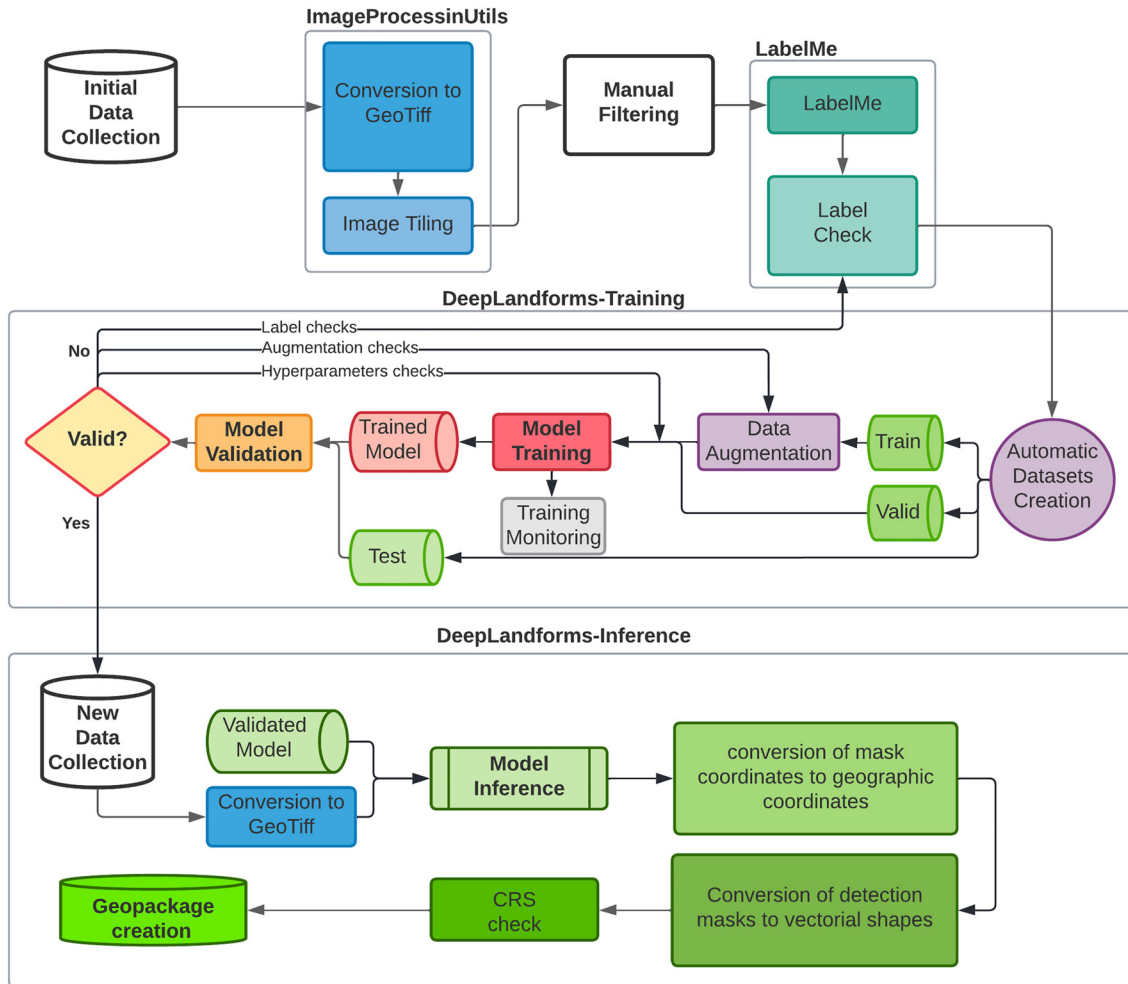


Figure 2. Flowchart of the complete workflow on which the DeepLandforms toolset relies.

*Labelme* Docker container, an open-source tool with a graphical user interface for creating segmentation labels (Wada, 2021). The third component is the DeepLandforms Docker container, which includes two Jupyter notebooks, both built on top of the Detectron2 library, *DeepLandforms-Training* and *DeepLandforms-Segmentation*. DeepLandforms-Training notebook is an implementation of Detectron2 Library's training components in a Jupyter notebook in which is possible to control all the main hyper-parameters mentioned in Text S1 in Supporting Information S1, such as Epochs, Learning rate, batch size and more. This notebook automatically splits the source data set in train, valid, and test sub-datasets and performs data augmentation on the train data set, randomly applying salt&pepper noise and blur to the images. After data augmentation, a class distribution pie chart is shown.

DeepLandforms-Segmentation notebook is an implementation of the Detectron2 Library's inference components. This notebook includes several custom functions which are used to compute the geographic coordinates of the detection masks by using the affine transform of the inferred image. Another dedicated function converts the masks into vectorial data and stores all the detections in a geopackage file. Additionally, we developed also a specific function to convert the detection masks into label files in COCO json format that can be directly used to perform new training sessions. This notebook can work also be used with Detectron2 models trained with other tools.

The fourth component is the *Tensorboard* Docker container, a simple utility for monitoring the training process.

All the components combined, requires at least 15 GB of free disk space in order to be installed and operational.

## 2.2. Detection Masks Conversion to Geo-Referenced Polygons

As mentioned in the introduction, all results obtained by Mask-R-CNN are image masks described with pixel coordinates that completely lack of any geospatial information. Therefore, it is necessary to convert the masks to geo-referenced polygons. This operation has been accomplished by developing a function based on a Python library named Rasterio (Gillies & others, 2021), which contains specific modules for spatial data manipulation by using each inferred image affine transform. The affine transform is a matrix that describes the geometrical properties of an image and contains the origin of the image (top left corner), its cell size, and geometrical distortion if present. By combining affine transform and mask coordinates, it is possible to retrieve the geographical coordinates of the masks. This operation also maintains the coordinate reference system of the source image. Notice that if the source image is not geo-referenced properly, the misplacement errors are propagated to the affine transform and to the final polygons. See Text S4 and Figure S3 in Supporting Information S1.

## 3. Pits/Skylight Proof-Of-Concept Use-Case

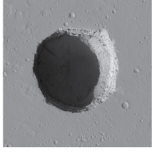
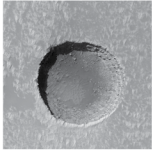
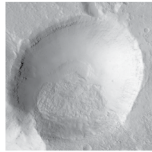

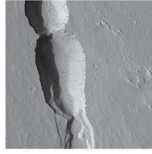
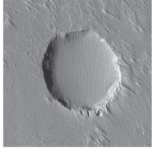
While this toolset is not specific to any landforms, we chose pits/skylights and craters as test landform.

Pits and skylights are depressions of the terrain characterized by an elongated to almost circular shape, flat rims and bottom, walls ranging from almost flat to very steep and, in some cases sub-vertical (Cushing et al., 2015; Cushing & Titus, 2010; U. Sauro, 2016; F. Sauro et al., 2020; van der Bogert & Ashley, 2015; Wyrick, 2004). On Earth, their formation mechanisms are commonly related to the collapse of the top of a subsurface cavity, caused by the chemical or mechanical erosion of the subsurface sediments. On other planetary bodies, such as Mars and the Moon, their formation mechanisms are still debated. As mentioned before, pits and skylights may have different shapes and dimensions on Earth and other planetary bodies (Cushing et al., 2015; Hong et al., 2015; F. Sauro et al., 2020; Sharma & Srivastava, 2021; Whitten & Martin, 2019), yet maintain almost all the characteristics. The classification proposed in Figure 3 is an expansion of the classification proposed by Cushing et al. (Cushing, 2017; Cushing et al., 2015) and is based only on a qualitative morphological analysis by observing the visual appearances of the features characteristic of pits and skylight, without taking into account morphometric properties. Performing only a qualitative morphological analysis may introduce misclassification errors because of the apparent similarities of different morphologies when particular conditions are met. For instance, strong similarities are common between Type-1b, Type-2a, and Type-4, especially when the solar incidence angle is low. The same errors may also occur between Type-1a and eroded craters and high solar incidence angle. To mitigate the occurrence of these errors, if a DTM is available, the best approach is to look at topographical profiles. This approach is described in Text S6 in Supporting Information S1, including visual examples Figures S4 to S7 in Supporting Information S1. Otherwise, it is common practice to perform a context-aware analysis of the surroundings of the target landform, looking for additional features and indicators, such as similar morphologies. It is also advised to look at other information like solar incidence angle, image acquisition angle, and more, all commonly embedded in the file metadata or in the ancillary file provided in the data archive.

While these additional analyzes are a common practice for whom performs the classification, standard convolutional neural networks are not yet capable of performing a context-aware feature extraction, thus their capabilities are constrained by the quality and quantity of the training data.

The most consistent and peculiar characteristic among pits/skylights that almost always differ greatly from craters is the presence of a raised rim. As previously mentioned, in craters it is common to find a bulge all along the rim, or in a specific direction that usually corresponds to the impact trajectory, while bulged rims in pits and skylights are almost completely absent or associated with previously existent landforms that can be visible also nearby to the pits and skylights.

The best method to evaluate the differences between pit and crater rims is to manually plot and evaluate DTM profiles but, since in most cases DTMs are not available, it is possible to evaluate them by plotting a profile along the maximum illumination direction of visible images. A detailed description of this method is presented in Text S6 in Supporting Information S1.

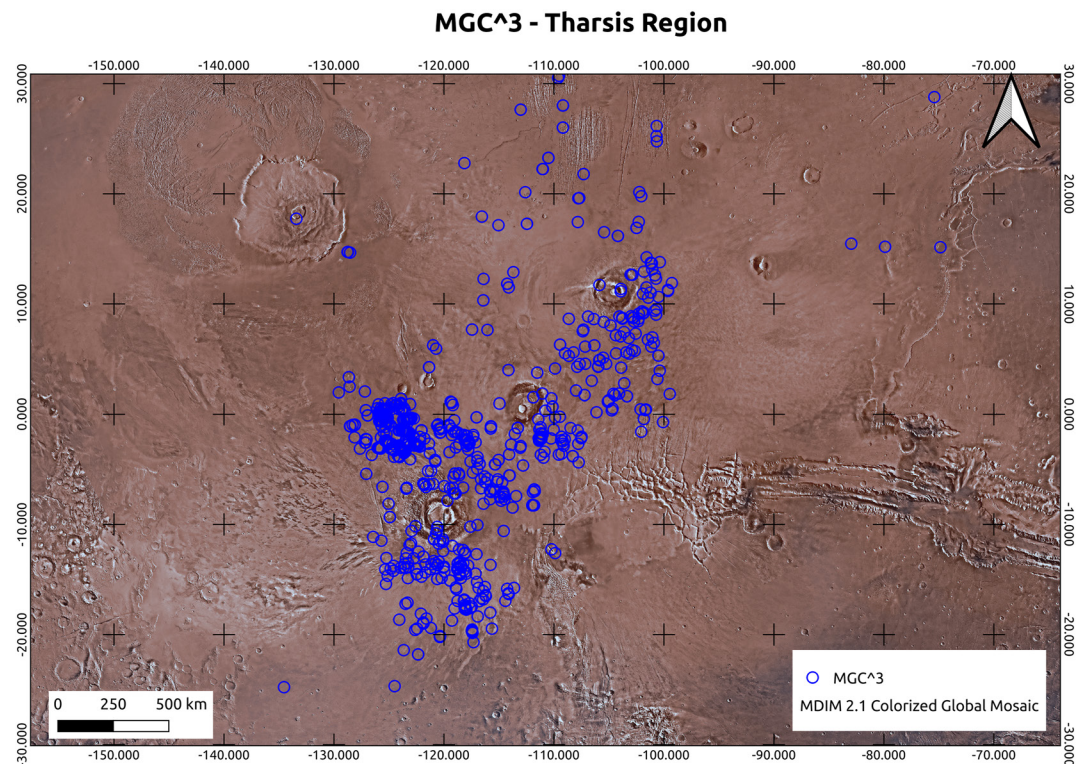
Image	ID	Description
	1a	Type 1a – Skylight with possible cave entrance characterized by quasi perfect circular shape, flat rim, no ejecta marks, and almost nonvisible bottom. When visible bottom is present, it is possible to see vertical to overhanging walls by the projected shadows and in some cases piles of debris at the center with conical upward shape. Often found isolated or in proximity of all other types, especially Type-4 and Types-2a-b.
	1b	Type 1b – Pit with possible relation to cave entrance and, or lava tube characterized by quasi circular shape, sub-vertical to vertical walls, almost flat rim, no ejecta marks, almost circular shape, and visible bottom. In some cases, it is possible to see circular marks of darker terrain on the floor, near the sub-vertical walls.
	2a	Type 2a – “Bowl” pit with uncertain connection to lava tubes or dikes characterized by a semicircular shape, almost flat rim, no ejecta marks, sloped walls and visible convex bottom. Often isolated or in connection with Type-3
	2b	Type 2b – Pit with uncertain connection to lava tubes or dikes characterized by a semi elliptical shape, almost flat rim, no ejecta marks, sloped walls and visible convex to flat bottom. Often isolated or in connection with Type-3
	3	Type 3 – Coalescent pits characterized by a mix of characteristics of Type-2a-b. Possible connection to lava tubes or dikes due to the alignment of Type-2a-b.
	4	Type 4 – Pit with possible connection to lava tubes or dikes due to the alignment of multiple similar shapes, characterized by a semicircular shape, almost flat rim, no ejecta marks, shallow to very shallow depth, sloped to sub-vertical walls and visible flat bottom. Often aligned with other Type-4 or in connection with Type-3 and Type-1a-b, rarely isolated.

**Figure 3.** Main types of pits/skylights that can be identified on Mars, also used as classes for labeling training data set, expanded from a previous work (Nodjoumi et al., 2021).

### 3.1. Region of Interest

Since our targets of interest are pits/skylights, we decided to collect data from a specific region of Mars named *Tharsis Region*. This region has its central coordinates at 0°N 260°E and is characterized by the presence of four of the largest shield volcanoes in the Solar System: Olympus Mons, Arsia Mons, Pavonis Mons, and Ascreus Mons. Considering the presence of these large shield volcanoes in this region and thus possible intact lava tubes, it is the best candidate region to look for possible cave entrances. Moreover, a previous work by Cushing et al. (Cushing, 2017) identified and published a database, the Mars Global Cave Candidate Catalog (MGC<sup>3</sup>) containing point location of thousands of pit/skylights landforms. Considering that the MGC<sup>3</sup>, was created and validated by analyzing manually several Context Camera (CTX) and HiRISE imagery, we decided to use it as a reference for the initial data selection and as a control data for all the analyzes performed in this and the previous work (Nodjoumi et al., 2021). A map showing the MGC<sup>3</sup> catalog over the *Tharsis Region* is reported in Figure 4.





**Figure 4.** MGC<sup>3</sup> over the Tharsis region.

## 3.2. Materials and Methods

### 3.2.1. Source Data Type

The data used in this work are mainly images acquired by image sensors operating in the visible (VIS) and Near InfraRed (NIR) spectrums on board of probes orbiting Mars, as shown in Table 1.

This data set is composed of images by HiRISE instrument and downloaded both as Reduced Data Record (RDR) and Experiment Data Record (EDR) format from public space archives such as PDS Geosciences Node Orbital Data Explorer (ODE) (PDS Geosciences Nodes, 2021).

### 3.2.2. Methodology

In order to validate all the packages, tools and the complete workflow, an intensive test has been performed on the above-mentioned pit, skylights landforms, including a generic set of craters for references and for testing the capability to discriminate those whose appearance resemble some types of pits.

### 3.2.3. Data Pre-Processing

EDR images have been processed initially to produce RDR version using USGS Integrated Software for Imagers and Spectrometers (ISIS) (Laura et al., 2021) and then converted into jpeg2000 (JP2) file format or GeoTiff file format using the *ImageProcessingUtils* container. We used a dockerized version of ISIS (Nodjoumi et al., 2022) to perform the EDR to RDR workflow available in Text S7 in Supporting Information S1.

**Table 1**

*The Data Set Used for Training and Testing Purposes Is a Selection of the Tharsis Region Images Acquired by the HiRISE Instrument*

Orbiter	Target	Instrument	Sensor type	Ground sampling resolution	Images
Mars Reconnaissance Orbiter (MRO)	Mars	High-Resolution Image Science Experiment (HiRISE)	Panchromatic VIS + NIR	Up to 0.30 m/pixel	~1,000

**Table 2**

*Comparison Between Approaches, Scaling Approach May Be Better for Analysis of Features at Regional Scale, While Tiling Approach May Be Preferred for Smaller Landforms*

Requirements	Limits	Compromises	Approach
Maintain context	Scaling to very low resolution may lead to huge loss of details	Limit the scaling to maintain discretization capabilities	Scaling approach
Maintain high discretization and avoid object splitting	Larger images produce several tiles proportional to the original image, objects may results split across several tiles	Limit the dimension of the tiles to avoid object splitting and keep the number of tiles low	Tiling approach

Computational requirements of Machine Learning and, more in particular of Deep Learning architectures for Computer Vision are strictly determined by image bands number, image resolution, image size, and data set size, which have a great impact especially during the training of the model. On the other hand, the impact on computation resources during the usage of the pre-trained model is lower. The Martian and lunar high-resolution images from HiRISE and LROC, are enormous in terms of data size, easily reaching 50,000 pixel height. These images require a lot more processing resources than those required for processing low-resolution images, especially if the aim is to make them compatible with Deep Learning tasks or to reduce the computational requirements.

A simple and easy approach would be the direct resizing of these images but, this is not always possible because there is a significant risk of losing the object's unique details or even worse introducing apparent similarity between two different objects.

A better approach is to divide the images into tiles of the desired resolution. Here there is no detail loss, since the original spatial resolution is preserved, but the number of images increase dramatically. The tiles need to be filtered out of by removing the tiles which do not contain any relevant features and then the remaining tiles need to label. for example, The HiRISE PSP\_004715\_1855\_RED image is  $30137 \times 76047$  pixels, so dividing it into  $\sim 512 \times 512$  pixels tiles results in more than  $\sim 8,700$  tiles. Even tiling into larger tiles is not always a workable approach. Such tiling may cause the loss of contextuality of the objects, or introduce difficulties during the labeling tasks, since the object may be split across multiple tiles.

In this situation, it is advised to define the requirements of the analysis and evaluate compromises between the approaches. In Table 2, we summarized the evaluation between scaling and tiling approach.

In the presented use case, a hybrid approach has been used: images spatial resolution has been scaled down to 5 m/pixel, then the resulting images have been sliced into tiles with 1,024 pixel max width or height. To achieve these specific tasks, the Docker container named *ImageProcessingUtils* was used.

The data set comprises 186 HiRISE RDR red channel images, see Table S4 in Supporting Information S1. Using only red channel images is due to the swath of 6 km cross-orbit and 20 km along-orbit at a nominal 300 km nominal orbit. In comparison, the Blue-Green and NIR images have a swath of 1.2 km cross-orbit.

Those images have been processed using the *ImageProcessingUtils* (Nodjoumi, 2021b) Docker container to convert from jpeg2000 file format (JP2) to GeoTiff and then resized to a common 5 m/pixel cell size, and tiled into more useable files with the largest side up to maximum 1,024 pixel.

All resulting images have been manually examined to filter out those which did not contain any landform relevant for the labeling steps, obtaining 486 labels. In Table 3, class distribution is summarized.

### 3.2.4. Data Labeling

Then, all the images have been ingested into the *LabelMe* Docker container to annotate all the pits, skylights, and some representative craters following the classification shown in Figure 3. At the end of the labeling task, it emerged that the labels were unbalanced, meaning that the data set does not contain an almost equal number of each class.

**Table 3**

*Class Distribution for the Source Data Set*

Type	No of labels
Crater	91
Type-1a	101
Type-1b	24
Type-2a	45
Type-2b	50
Type-3	42
Type-4	133

*Note.* Class unbalance is clearly visible as Type-1b, Type-2a, Type-2b, Type-3 are underrepresented.

Since the collection and processing of newer images containing more landforms of the unbalanced classes was not workable at the time of analysis, a simpler approach was chosen and comprise a reduction of the classes by grouping into similar ones, doing so resulted in only four classes, Type-1, containing -1a and -1b, Type-2, containing -2a and -2b, Type-3, Type-4.

### 3.2.5. Data Augmentation

Since the initial data set was rather small and unbalanced, containing less than an average of 70 labels per class, we prepared two additional python scripts to further increase and balance the data set. The first python script, *lbl extractor.py*, extract all the labels from the initial data set and save both the image and the label file in a new folder and create a geopackage containing all the information of the extracted labels, including the geometry. Then, using the *ImageProcessingUtils* Docker, we downscale the original images at different resolutions: 0.5, 1, and 3 m/pixel. Finally, we used the geopackage generated by the first script and, using the second python script, *lbl replicator.py*, we extracted the same original labels from all the new datasets.

Since all these labels were essentially the same, with the resolution as the only major difference, we implemented an additional step of data augmentation directly in the *DeepLandforms-Training* notebook.

This step was executed after splitting the data set into train, valid and test sub-datasets. The script randomly applies blur, salt&pepper noise effects.

Last, in order to reduce the strong class imbalance, we merged all subtypes for every class.

### 3.2.6. Data Training

After concluding the data set preparation, we used the *DeepLandforms-training* notebook to perform several training sessions using different combination and values for learning rate, batch size, and training epochs parameters. These parameters directly influence the training of the model. For instance, the learning rate (lr) affects the intensity of errors correction of the weights during training (small values of learning rate means small weights adjustments), the batch-size correspond to the quantity of images trained concurrently (larger batch size requires more processing memory and more time), and epochs affect both the speed and the overall accuracy (*Detectron2. Config—Detectron2 0.6 Documentation, 2022*).

The ranges of the main training parameters are summarized in Table S3 in Supporting Information S1. We have also used a different combination of classes and datasets to improve the results and mitigate over-fitting, as better discussed in the results chapter.

We used the *mask\_rcnn\_R\_50\_FPN\_3x* model configuration as, according to Detectron2's model zoo, it is reported to have the best-balanced results/training requirements ratio.

To evaluate the stability and scalability and the performance of the tool, we executed the above training on two different computers with Ubuntu Linux as the operating system and NVIDIA GPU card. Because of the high variability of hardware components and operating systems available, we could not test DeepLandforms and Detectron2 in other types of machines.

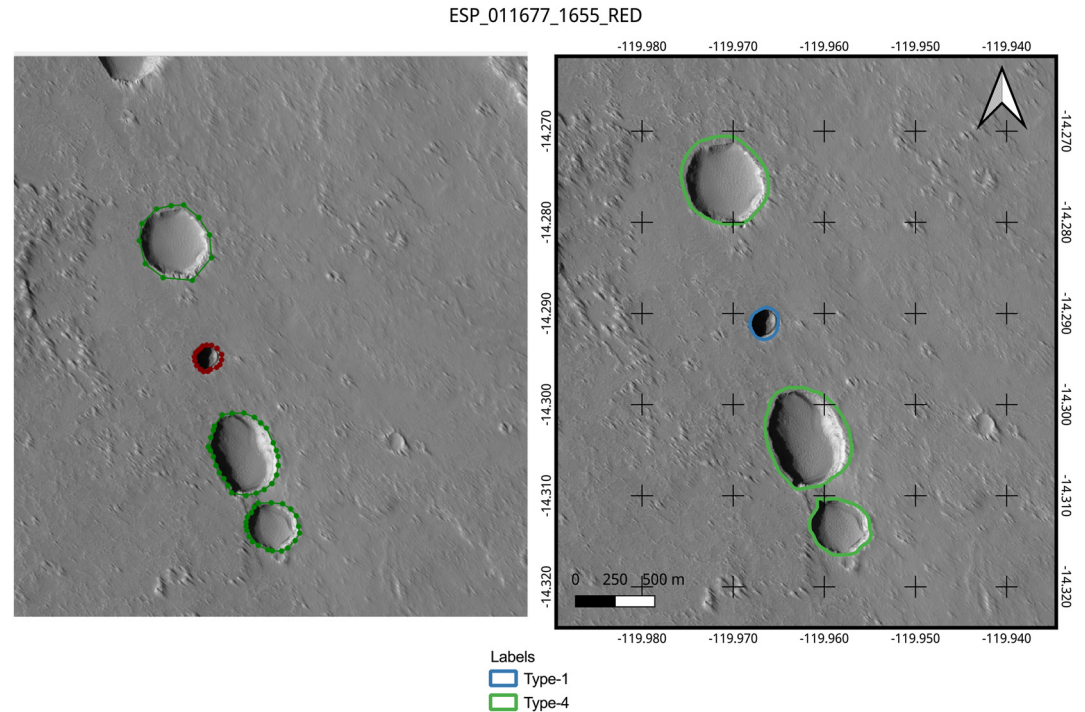
### 3.2.7. Training Monitoring

All the training sessions were monitored using the *Tensorboard* Docker container to evaluate the progression and the performance of the training sessions.

### 3.2.8. Training Evaluation

At the end of all the training sessions, we evaluated all the models by using them on the test data and by visualizing the training metrics in the *tensorboard* Docker as represented in Figures 6–8.

The main metric used to evaluate object detection and segmentation models is *mean Average Precision* (mAP), that is a comprehensive evaluation of the performance of the model. mAP metric, considers three sub-metrics: *precision* (accuracy of the predictions as a ratio between True Positive and False Positive), *recall* (capability to retrieve all positive predictions as a ratio between True Positive and False Negative), and *Intersection over Union* (IoU, a measure of the overlap between the predicted bounding box) and the ground truth bounding box. Commonly, for all major model configurations and frameworks, like Detectron2, developers periodically release



**Figure 5.** Comparison between ground truth labeled image used in training (left) and inferred labeled image (right). The major difference is in the density of the points of the shape, where in the inferred image are far denser than those of the ground truth.

a set of benchmark metrics that are computed by running each model configuration with very large datasets (e.g., COCO data set). Detectron2's benchmark metrics are available on the official GitHub page (Y. Wu et al., 2019).

We tested the trained model on the valid data set, and then the results were loaded into the *LabelMe* Docker container to check if the labeled objects are detected and labeled correctly, as shown in Figure 5.

#### 4. Results

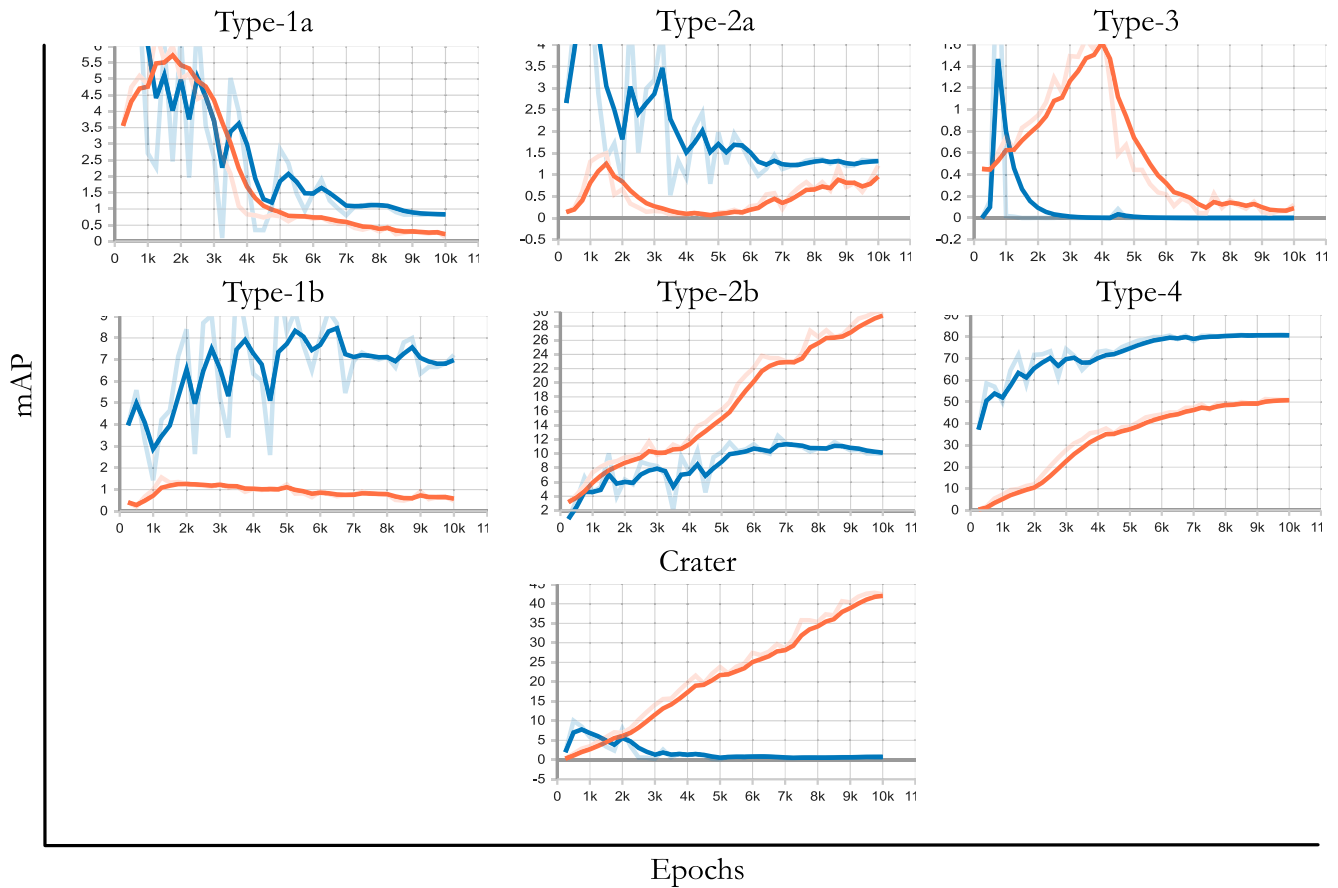
Herein are described the results obtained after re-training Mask-R-CNN models on a custom data set of HiRISE images containing pit/skylights' landforms. All the configuration parameters, the components of DeepLandforms, including additional descriptions of the data pre-processing and labeling components, the training and inference Jupyter notebooks, and the obtainable results are available in Text S3, S4, S5, S6, and S7 and Tables S2, S3, and S4 in Supporting Information S1. In the first training session, we trained all the sub-classes using the whole data set, obtaining poor results for all the classes, as shown in Figure 6. Since this is mostly caused by class unbalanced and small data set, we decided to combine the sub-classes for all subsequent training sessions, reducing the classes to Type-1, Type-2, Type-3, Type-4, Crater.

We performed new training sessions using different combinations of the same data set and combined classes (train\_532105\_1\_2+3\_4\_5 and train\_321\_cls\_1\_2\_3\_4 in Figure 7, where 532,105 and 321 correspond to the resolution used) but the results did not improved. We suspected that within this data set, the variability between all labels of each class is low, so we decided to remove the Crater class and combine class 2 with class 3 before training the model again. Figures 7 and 8 shows combined results and evaluation metrics relative to six training runs, visualized using *tensorboard* Docker container.

Using combined and simplified classes, mAP increased dramatically. The results were also consistent across multiple runs and while training with smaller data set (e.g., train\_321\_cls\_1\_2+3\_4). These results further improved when we used only Craters and Type-1 classes, as show in Figure 8.



Example of Mean Average Precision (mAP) of the Fast-R-CNN component - 7 classes



**Figure 6.** Example of Mean Average Precision (mAP) of the Fast-R-CNN component (object detection) obtained from two training session using the same data set and 7 classes. The poor results and high variability of the mAP is mostly due to class imbalance and low data set diversity. Each color corresponds to different training session. Higher mAP correspond to better results.

To further evaluate the training of the models and check whether over-fitting or underfitting occurred, we plotted the Total/Validation Loss as shown in Figure 9.

Total and validation loss are metrics computed during the training and are generated by assessing the cumulative errors during the training on train (total loss) and valid (validation loss) datasets. Both metrics are fundamental to evaluate the overall quality of the training and to visualize if over-fitting or under-fitting occurred. Examples of over-fitting and under-fitting are presented in Figure S2 in Supporting Information S1.

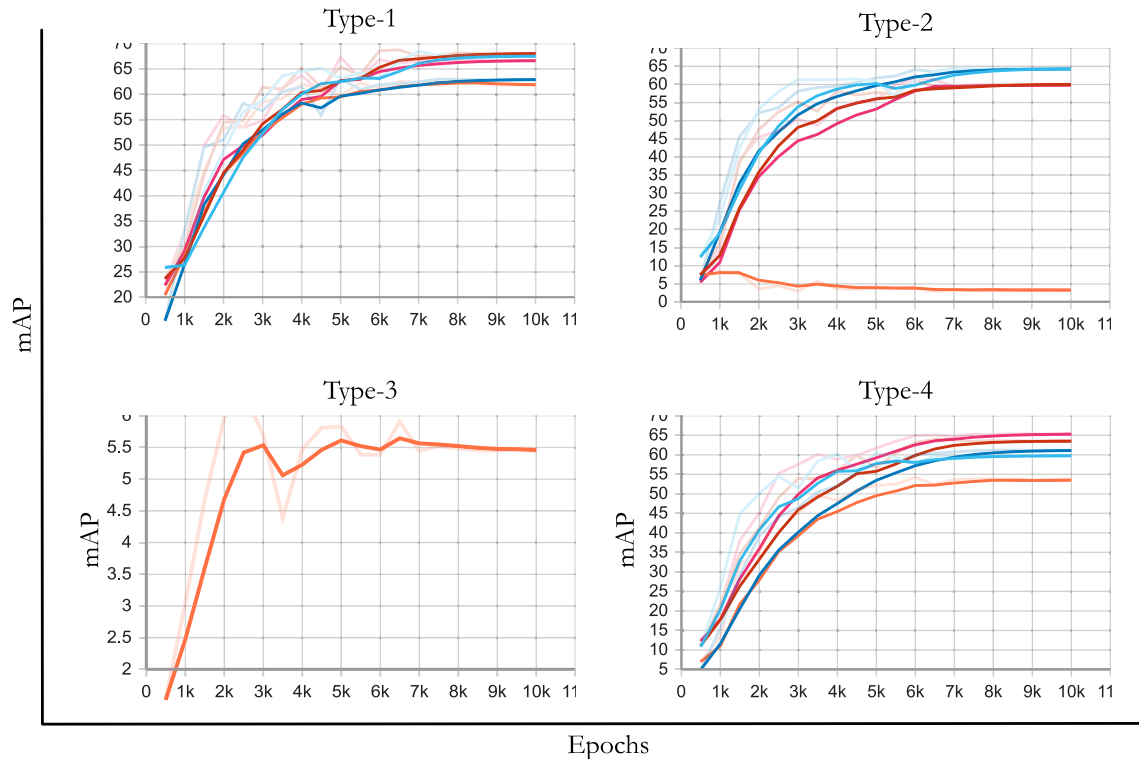
Finally, we used the trained model to predict and map the trained landforms on some of the original images with good results. We used QGIS software, to import and visualize both tested images and the geopackage file containing the results as shown in Figures 10, 11, and 12. Despite these detections seems good, it is necessary to consider that Figures 10 and 11 are part of the training data set, while Figure 12 is new.

Despite the good values of mAP and accuracy, there are several landforms missed completely by the model, as is possible to see in Figure 11.

Notice that, in all the processed images, there are different misalignments between the MGC<sup>3</sup> points and the HiRISE or CTX Images. The cause of this discrepancy has not been identified yet but is probably due to the positional uncertainty introduced during the map projection of the EDR and the use of uncontrolled data. To greatly reduce these errors and to have a more accurate positioning of the images, is strongly advised to co-register all the images to a common basemap. In Figure 12, another clear example of position error is showed.



Example of Mean Average Precision (mAP) of the Fast-R-CNN component - 4 classes



**Figure 7.** Mean Average Precision (mAP) of the Fast-R-CNN component (object detection) relative to 6 training runs. All the runs with high values of mAP corresponds to those trained using a data set in which Crater class is removed and Type-2/Type-3 are combined. The only run with poor values is the one trained with all classes. Y axis correspond to mAP while X are the train epochs. Each color corresponds to different training session. Higher mAP correspond to better results.

## 5. Discussion

### 5.1. DeepLandforms Toolset

Using *DeepLandforms* toolset, it was possible to perform all the steps necessary to train and use Deep Learning instance segmentation models without the necessity of relying on separate tools, nor install several python environments and packages. The only exception was the conversion of the source EDR to map-projected RDR that can only be performed using ISIS.

With the *ImageProcessingUtils* Docker container, it was possible to prepare the initial base data set by scaling and tiling the source RDR images. Then, with the *labelme* Docker container, we labeled all the images for instance segmentation.

Using *DeepLandforms* Docker container, we performed both the training sessions with different combination of training parameters and the analysis of newer images using the trained model.

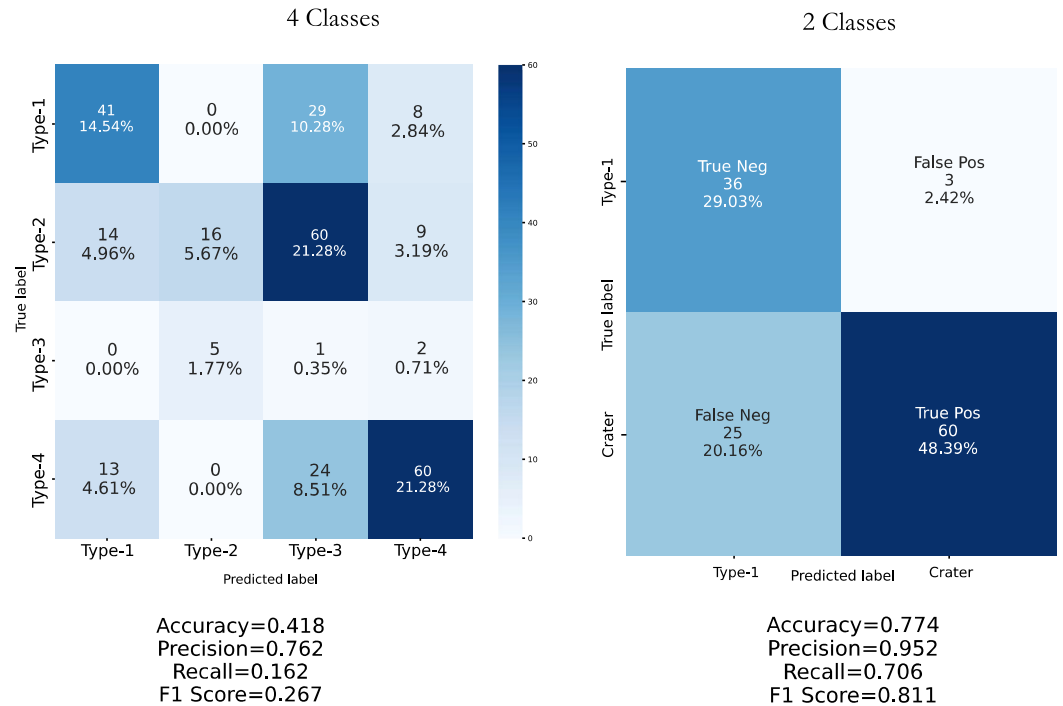
Finally, with *tensorboard* Docker container, it was possible to monitor and compare all the training metrics.

The results that can be obtained using *DeepLandforms* are highly dependent on several aspects.

- Quality and quantity of the data set: more and better data are necessary to better generalize the unique characteristics of the target classes,
- Quality of the labels: accurate labels grant better segmentations, since it is a pixel-wise analysis,
- Tuning of hyper-parameters: in addition to the base hyper-parameters (learning rate, batch-size, epochs) there are a lot more parameters that can be tuned to improve the training.

A summary of assets and liabilities is presented in Table 4.

Comparison of confusion matrix heatmaps between models trained with different number of classes



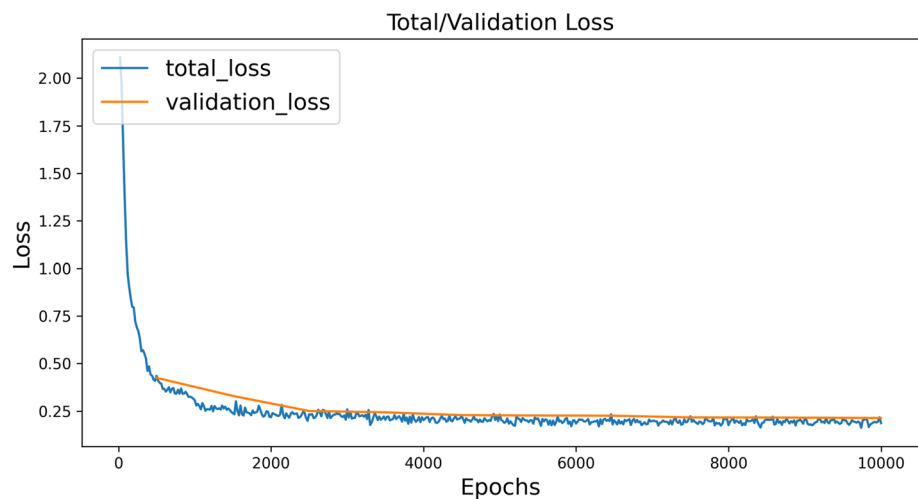
**Figure 8.** Heatmaps displaying the confusion matrix obtained on the test data set for the model trained with 4 classes (left) and with 2 classes (right).

## 5.2. Pit/Skylight Use-Case

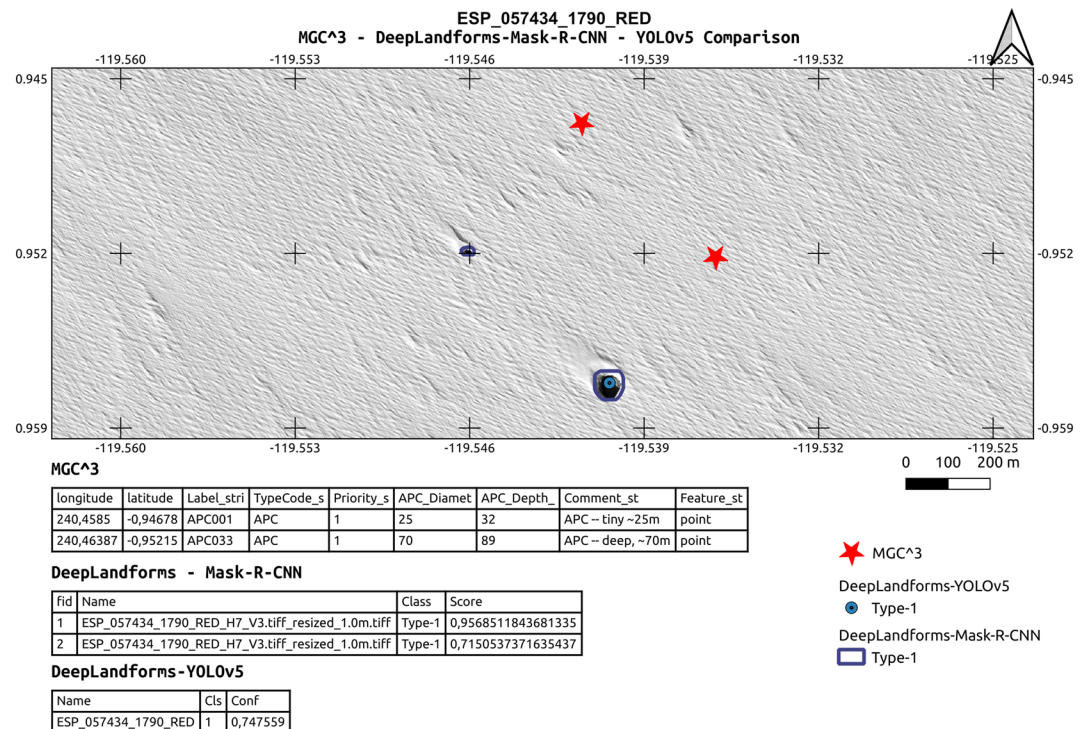
The proof-of-concept use case of pit/skylight detection on Mars was extremely useful to evaluate DeepLand-forms' workflow.

### 5.2.1. Image Pre-Processing

Data set composition was the most time-consuming task since it included all image pre-processing steps that required also a lot of computing time. First, we analyzed MGC<sup>3</sup> to identify high-density pitted areas, then we



**Figure 9.** Plot of Total/Validation Loss of the train run 532105\_1\_2+3\_4. The validation curve follows very well the total loss curve, meaning that the model trained without over-fitting or under-fitting.



**Figure 10.** Example of detection on High Resolution Imaging Science Experiment Red channel image and comparison between MGC^3, DeepLandforms-YOLOv5 object detection and DeepLandforms-Mask-R-CNN instance segmentation. Tables show attributes of fields in the shapefiles.

collected relative EDR images from data archives and converted from USGS standards to geospatial GeoTiff. Once converted, we evaluated and validated all processed RDR images.

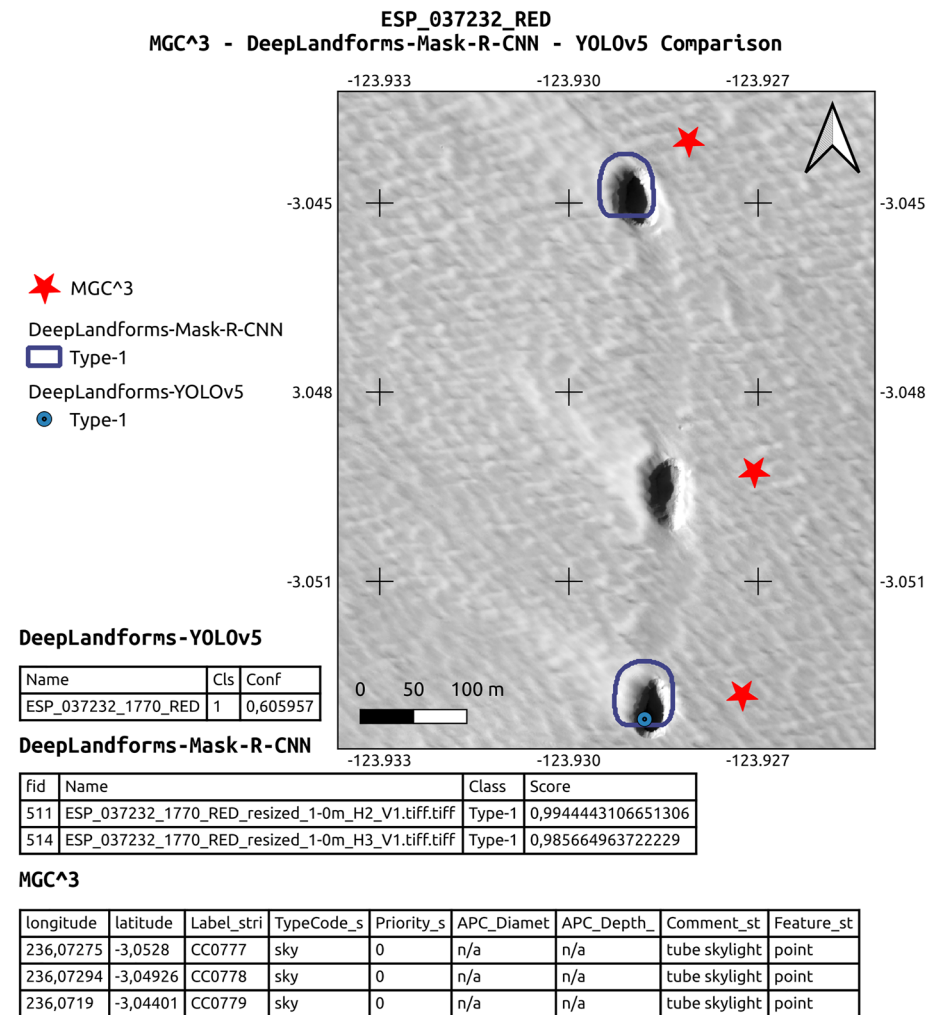
Next, we used *ImageProcessingUtils* Docker container to reduce the size of all images by tiling and down-sampling them at different cell resolutions. This step was highly demanding in computer resources since it required a few hundreds of GB of disk space and 3 days to convert all the images to downsampled and tiled GeoTiffs, using a 14 cores, 24 threads machine equipped with 32 GB of ram. The manual selection step took approximately 2 days, while the labeling required 1 week.

### 5.2.2. Model Training and Evaluation

We executed all training sessions in parallel on three different computers, using the same parameters and data set, Table S5 in Supporting Information S1, requiring an average of 6 hr for each training. Using *tensorboard* Docker container was possible to monitor the training, helping to abort prematurely the training in the occurrence of terrible metrics (e.g., mAP not increasing or decreasing, low accuracy). For instance, we aborted the `train_532105_1_2+3_4_5` session after 5,000 epochs. *Tensorboard* was also used to compare all training metrics relative to all trained models, as shown in Figures 6–8. While performing all the training sessions, we found that when training five or less classes, a minimum of 1,000 labels for training and 250 labels for validation are necessary, while for training more than five classes more labels are necessary. These values increase when trained classes are very similar. All well-trained models, tested on their respective test data, could detect correctly almost all landforms, although several misclassification errors and few missing detections. We expected these kinds of results since the original data set is small, while the final training data set is mostly composed of the augmented version of the same source data.

### 5.2.3. Remarks on Pit/Skylights

An automated or semi-automated approach as the one proposed in this work, compared to the manual mapping, may be a game-changer, providing robust processing workflows for generate high-end data in compliance with



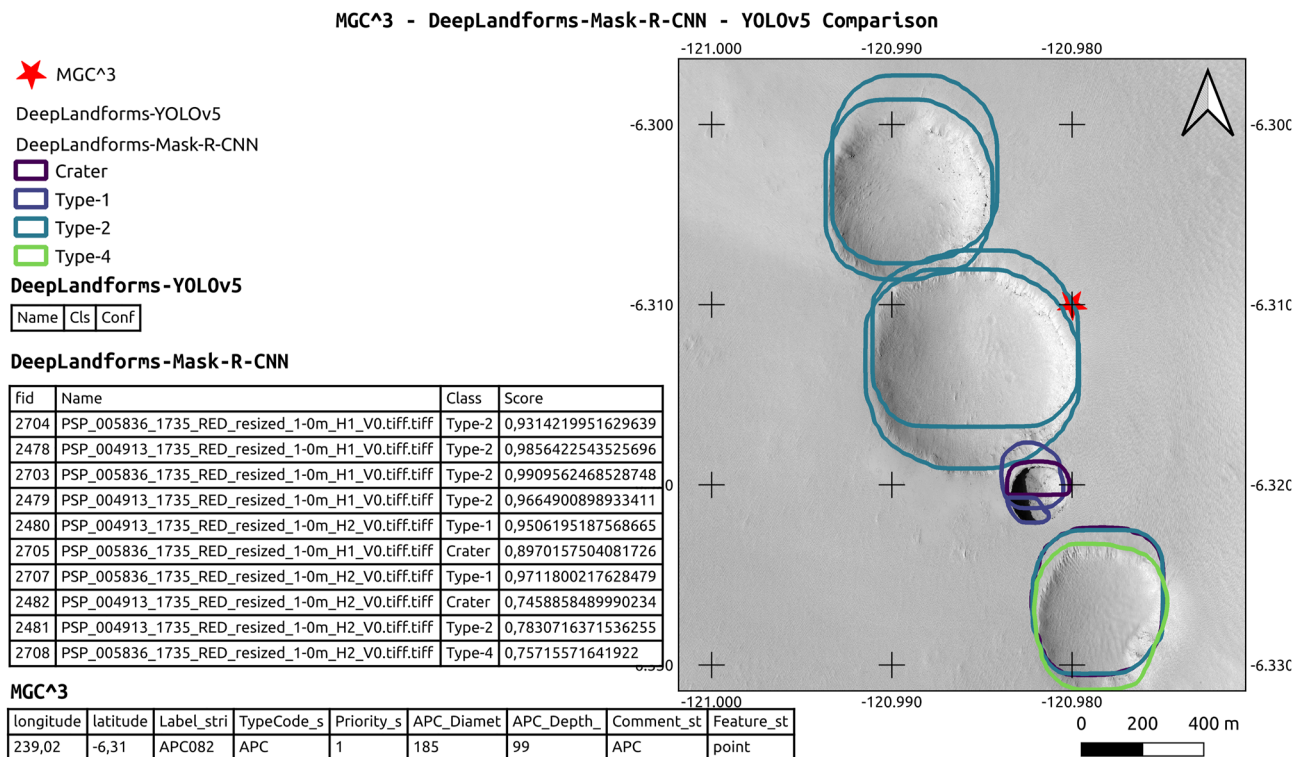
**Figure 11.** Example of detection on High Resolution Imaging Science Experiment Red channel image and comparison between MGC^3, DeepLandforms-YOLOv5 object detection and DeepLandforms-Mask-R-CNN instance segmentation. Tables show attributes of fields in the shapefiles.

the OGC standards, for map productions at planetary scale, with the enormous advantage of relaying the most time-consuming task of data pre-process and first analysis to computer time instead of human-time.

The analysis presented in this work, if expanded to a large data set, and if implemented with morphometrical analysis, may improve the knowledge of the spatial distribution of skylights, pits, and pit chains, including those already known and described, providing a detailed wide map that can be further integrated with morphometric analyzes.

## 6. Conclusions

The advantages and improvements in data analysis provided by machine learning are undoubtful and constantly expanding in more and more sectors, especially in remote sensing of Earth and Space. With an exponential amount of fast-growing available datasets, newer and faster methods are necessary to perform a continuous stream of analyzes, and with a plethora of publications, works, architectures and unconnected tools available, that are mainly *accessible* by everyone, albeit not *useable* by not insiders, is also necessary to make those available for the wider audience, especially those who are involved in the analyzes of data but are not specialized in the machine learning.



**Figure 12.** Example of detection on High Resolution Imaging Science Experiment Red channel image and comparison between MGC<sup>3</sup>, DeepLandforms-YOLOv5 object detection and DeepLandforms-Mask-R-CNN instance segmentation. Multiple misclassification and segmentation error occurs. Classification errors, such as Type-1/Crater are mostly caused by the small training data set. Segmentation errors are caused by both the small data set and by inference performed on tiles. For instance, Type-1 and Type-2 have straight horizontal lines that correspond to the edge of the tile. This specific error can be mitigated by using larger tiles or by implementing a sliding-window analysis. Tables show attributes of fields in the shapefiles.

*DeepLandforms* toolset, presented in this work, may be a forerunner, and a tentative to lead an easier approach well suitable both for first-time users and advanced users.

Despite this toolset is at its first release, and still in development, it may help to further improve the mapping process in faster and robust ways.

Although this use-case is a proof-of-concept, skylight, pits and pit chains are an extremely interesting type of landforms that can be observed on almost all rocky planets and moons of the Solar System.

Formation mechanisms are commonly related to volcanic and tectonic processes but are still debated, moreover it is still not clear whether such formation mechanisms are the same on all planetary bodies in which those landforms are observed, especially since there are very similar and common morphological characteristics among all observations. If it is the case of common formation mechanisms, this implies that there should be shared geological properties and settings among those bodies, thus common geological history.

**Table 4**  
*Tabulated Assets and Liabilities of the Toolset Presented in This Work*

Assets	Liabilities
Almost ready-to-use	Not compatible with every platform and hardware configuration
Semi-automated approach	Require intensive user supervision in the initial phase and during preliminary evaluation
Large data volume processing capabilities	Depends on the machine in which is running
Possibly to use results for further correlation with other data	
Wide adaptability to different landforms	May not be compatible with every landform type, depending on the training data



Further on, skylights and some pits may have access to caves as observed on Earth analogs, and hypothesized on Mars and the Moon (Hong et al., 2015), such as those found in large shield volcanoes (Léveillé & Datta, 2010; F. Sauro et al., 2020). Presence of accessible caves on other planets and moons has a huge importance for space exploration since those cave may contain traces of life, both past and potentially present, as some extremophile bacteria and other smaller life-form may have found shelter from harsh surface condition and cosmic radiations (NASA, 2021). Moreover, caves are considered as good candidates for future human habitation outposts (Cushing & Titus, 2010; Pipan & Culver, 2019), and also are an excellent window on subsurface structure, thus providing valuable information for understanding the geological settings and evolution of the area and potential direct access to mineral resources (Blamont, 2014).

To explore the above-mentioned targets and objectives, is necessary an accurate and global scale mapping of skylight, pit and pit chains, in order to better understand the spatial distribution of such landforms and correlate their presence with other geological and non-geological features and settings.

For instance, since pit chains may be related to the presence of lava tubes or dikes (Ferrill et al., 2011; Whitten & Martin, 2019; Wyrick, 2004), mapping pits could lead to new understandings of lava tube distribution, thus to better knowledge of volcanic processes involved, even across planets and moons. Isolated pits with no surrounding other morphological evidence may indicate the presence of a deep buried lava tube or cavity originating from other processes.

It is also possible to compare the distribution of such landforms with structural maps or other features that may be interconnected (Ferrill et al., 2004, 2011).

Another advantage is connected to planetary human mission planning, since the availability of geomorphological maps, even if not at highest resolution possible, may lead to the identification of better scientific targets or path planning in the case of rovers.

## 7. Further Development

Further development includes implementation of sliding window to improve further the segmentation of large images without pre-tiling them, the integration with GIS statistics such as the parametrization of the detected shapes, including cross-analysis of different data types such as DTMs in order to improve the quality of the results including eventually volume estimation, or integration with hyperspectral data to retrieve a mineral composition of the surface.

Another development could integrate the workflow with the SfS technique (Alexandrov & Beyer, 2018; Lohse et al., 2006; Micheletti et al., 2015) in order to extract depth and thus volume information where DTMs are not available.

Moreover, this toolset is not specific to any planetary body nor specific landforms, thus is compatible with every planet or moon imagery, if provided images are geo-referenced and the corresponding reference system is passed to the tool.

## Conflict of Interest

The authors declare no conflicts of interest relevant to this study.

## Data Availability Statement

The original data used for this study are available at publicly data archive NASA PDS Geoscience Node ODE (PDS Geosciences Nodes, 2021). Data sets for this research are available in these in-text data citation references (Nodjoumi, 2021a) with license GPLv2+ and available at: <https://doi.org/10.5281/zenodo.7351391>. Software for this research is available in these in-text data citation references (Nodjoumi, 2021c): with license GPLv2+ and available at: <https://doi.org/10.5281/zenodo.7488867>. All base images of the figures have been prepared using QGIS software 3.16 LTS and then processed with Affinity Publisher 1.1.

## Acknowledgments

We thank Dr. Erica Luzzi for providing comments on the manuscript. This study is within the Europlanet 2024 RI and EXPLORE project, and it has received funding from the European Union's Horizon 2020 research and innovation programme under grant agreement 871149 and 101004214. Open Access funding enabled and organized by Projekt DEAL.

## References

- Acharya, G., De Smedt, F., & Long, N. T. (2006). Assessing landslide hazard in GIS: A case study from Rasuwa, Nepal. *Bulletin of Engineering Geology and the Environment*, 65(1), 99–107. <https://doi.org/10.1007/s10064-005-0025-y>
- Alexandrov, O., & Beyer, R. A. (2018). Multiview shape-from-shading for planetary images. *Earth and Space Science*, 5(10), 652–666. <https://doi.org/10.1029/2018EA000390>
- Allemand, P., Delacourt, C., Gasperini, D., Kasperski, J., Pothérat, P., & Varrel, E. (2011). Thirty years of evolution of the Sedrun landslide (Switzerland) from multitemporal orthorectified aerial images, differential digital terrain models and field data. *International Journal of Remote Sensing Applications*, 5(12), 7–2802. <https://doi.org/10.3390/rs122785>
- Alonso, E. E., Pinyol, N. M., & Puzrin, A. M. (2010). Catastrophic slide: Vaiont landslide, Italy. In E. E. Alonso, N. M. Pinyol, & A. M. Puzrin (Eds.), *Geomechanics of failures. Advanced topics* (pp. 33–81). Springer Netherlands. [https://doi.org/10.1007/978-90-481-3538-7\\_2](https://doi.org/10.1007/978-90-481-3538-7_2)
- Anderson, J., & Lee Soltzes, D. (2003). USGS Isis: Logical Cube format guide. <https://isis.astrogeology.usgs.gov/>
- Aye, K.-M., Schwamb, M. E., Portyankina, G., Hansen, C. J., McMaster, A., Miller, G. R. M., et al. (2019). Planet Four: Probing springtime winds on Mars by mapping the southern polar CO<sub>2</sub> jet deposits. *Icarus*, 319, 558–598. <https://doi.org/10.1016/j.icarus.2018.08.018>
- Bardabelias, N., Holt, J., & Christoffersen, M. (2020). *Potential detection of Martian lava tubes from Mars global cave candidate catalog skylight locations using SHARAD* (Vol. 2197). 3rd International Planetary Caves Conference.1068.
- Barlow, N. G., Ferguson, S. N., Horstman, R. M., & Maine, A. (2017). Comparison of central pit craters on Mars, Mercury, Ganymede, and the Saturnian satellites. *Meteoritics & Planetary Science*, 52(7), 1371–1387. <https://doi.org/10.1111/maps.12857>
- Barrett, A. M., Balme, M. R., Woods, M., Karachalios, S., Petrocelli, D., Joudrier, L., & Sef-ton-Nash, E. (2022). NOAH-H, a deep-learning, terrain classification system for Mars: Results for the ExoMars Rover candidate landing sites. *Icarus*, 371, 114701. <https://doi.org/10.1016/j.icarus.2021.114701>
- Benedix, G. K., Lagain, A., Chai, K., Meka, S., Anderson, S., Norman, C., et al. (2020). Deriving surface ages on Mars using automated crater counting. *Earth and Space Science*, 7(3). <https://doi.org/10.1029/2019EA001005>
- Blamont, J. (2014). A roadmap to cave dwelling on the Moon and Mars. *Advances in Space Research*, 54(10), 2140–2149. <https://doi.org/10.1016/j.asr.2014.08.019>
- Bridge, J., & Demicco, R. (2008). Earth surface processes, landforms and sediment deposits (p. 835).
- Brierley, G., Fryirs, K., Reid, H., & Williams, R. (2021). The dark art of interpretation in geomorphology. *Geomorphology*, 390, 107870. <https://doi.org/10.1016/j.geomorph.2021.107870>
- Brust, C. A., Käding, C., & Denzler, J. (2019). Active learning for deep object detection. *VISIGRAPP 2019—Proceedings of the 14th International Joint Conference on Computer Vision, Imaging and Computer Graphics Theory and Applications*, 5, 181–190. <https://doi.org/10.5220/0007248601810190>
- Cahalan, M. D., & Milewski, A. M. (2018). Sinkhole formation mechanisms and geostatistical-based prediction analysis in a mantled karst terrain. *CATENA*, 165, 333–344. <https://doi.org/10.1016/j.catena.2018.02.010>
- Chappaz, L., Sood, R., Melosh, H. J., Howell, K. C., Blair, D. M., Milbury, C., & Zuber, M. T. (2017). Evidence of large empty lava tubes on the Moon using GRAIL gravity: Evidence of Lunar Lava Tubes from GRAIL. *Geophysical Research Letters*, 44(1), 105–112. <https://doi.org/10.1002/2016GL071588>
- Chen, M., Lei, M., Liu, D., Zhou, Y., Zhao, H., & Qian, K. (2017). Morphological features-based descriptive index system for lunar impact craters. *ISPRS International Journal of Geo-Information*, 7(1), 5. <https://doi.org/10.3390/ijgi7010005>
- Cruikshank, D. P., & Wood, C. A. (1972). Lunar rilles and Hawaiian volcanic features: Possible analogues. *The Moon*, 3(4), 412–447. <https://doi.org/10.1007/BF00562463>
- Cushing, G. E. (2017). *Mars global cave candidate catalog (MGC3)[abstract 3708]*. *Astrobiology science Conference*. Lunar and Planetary Institute. Retrieved from <https://www.hou.usra.edu/meetings/abscon2017/Pdf/3708.Pdf>
- Cushing, G. E., Okubo, C. H., & Titus, T. N. (2015). Atypical pit craters on Mars: New insights from THEMIS, CTX, and HiRISE observations: Atypical pit craters on MARS. *Journal of Geophysical Research: Planets*, 120(6), 1023–1043. <https://doi.org/10.1002/2014JE004735>
- Cushing, G. E., & Titus, T. N. (2010). Caves on Mars: Candidate sites for astrobiological exploration. *Astrobiology Science Conference*, 2–3.
- Cushing, G. E., Titus, T. N., Wynne, J. J., & Christensen, P. R. (2007). THEMIS observes possible cave skylights on Mars. *Geophysical Research Letters*, 34(17), L17201. <https://doi.org/10.1029/2007GL030709>
- De Blasio, F. V. (2011). Landslides in Valles Marineris (Mars): A possible role of basal lubrication by sub-surface ice. *Planetary and Space Science*, 59(13), 1384–1392. <https://doi.org/10.1016/j.pss.2011.04.015>
- Díaz Michelena, M., Kilian, R., Baeza, O., Rios, F., Rivero, M. Á., Mesa, J. L., et al. (2020). The formation of a giant collapse caprock sinkhole on the Barda Negra plateau basalts (Argentina): Magnetic, mineralogical and morphostructural evidences. *Geomorphology*, 367, 107297. <https://doi.org/10.1016/j.geomorph.2020.107297>
- DiPietro, J. A. (2013). The Tortoise and the Hare. *Landscape Evolution in the United States*, 3–14. <https://doi.org/10.1016/B978-0-12-397799-1.00001-4>
- Docker overview. (2021). Docker documentation. Retrieved from <https://docs.docker.com/get-started/overview/>
- Duhart, P., Sepúlveda, V., Garrido, N., Mella, M., Quiroz, D., Fernández, J., et al. (2019). The santa Lucía landslide disaster, Chaitén-Chile: Origin and effects (p. 9).
- Dundar, M., Ehlmann, B. L., & Leask, E. K. (2019). Machine-learning-driven new geologic discoveries at Mars rover landing sites: Jezero and NE Syrtis. ArXiv:1909.02387 [Astro-Ph, Stat]. Retrieved from <http://arxiv.org/abs/1909.02387>
- ESRI technical document. (1998). ESRI shapefile technical description. Retrieved from <https://www.esri.com/content/dam/esrisites/sitecore-archve/Files/Pdfs/library/whitepapers/pdfs/shapefile.pdfhttps://www.esri.com/content/dam/esrisites/sitecore-archve/Files/Pdfs/library/whitepapers/pdfs/shapefile.pdf>
- Ferrill, D. A., Wyrick, D. Y., Morris, A. P., Sims, D. W., & Franklin, N. M. (2004). Dilational fault slip and pit chain formation on Mars. *Geological Society of America Today*, 14(10), 4. [https://doi.org/10.1130/1052-5173\(2004\)014<4:DFSAPC>2.0.CO;2](https://doi.org/10.1130/1052-5173(2004)014<4:DFSAPC>2.0.CO;2)
- Ferrill, D. A., Wyrick, D. Y., & Smart, K. J. (2011). Coseismic, dilational-fault and extension-fracture related pit chain formation in Iceland: Analog for pit chains on Mars. *Lithosphere*, 3(2), 133–142. <https://doi.org/10.1130/L123.1>
- Geomorphological mapping. (2013). *Geomorphological Techniques* (p. 10).
- Ghorbanzadeh, O., Blaschke, T., Gholamnia, K., Meena, S., Tiede, D., & Aryal, J. (2019). Evaluation of different machine learning methods and deep-learning convolutional neural networks for landslide detection. *Remote Sensing*, 11(2), 196. <https://doi.org/10.3390/rs11020196>
- Gillies, S., & others (2021). Rasterio: Geospatial raster I/O for Python programmers. Mapbox <https://github.com/rasterio/rasterio>
- Grace, R. K., Anitha, J., Sivaramkrishnan, R., & Sivakumari, M. S. S. (2021). Crop and weed classification using deep learning (Vol. 4).

- Grant, J. A., Irwin, R. P., Grotzinger, J. P., Milliken, R. E., Tornabene, L. L., McEwen, A. S., et al. (2008). HiRISE imaging of impact megabreccia and sub-meter aqueous strata in Holden Crater, Mars. *Geology*, *36*(3), 195. <https://doi.org/10.1130/G24340A.1>
- Greeley, R. (1971). Lava tubes and channels in the lunar Marius Hills. *The Moon*, *3*(3), 289–314. <https://doi.org/10.1007/BF00561842>
- Guellini, L., Rossi, A. P., Forget, F., Marinangeli, L., Lauro, S. E., Pettinelli, E., et al. (2018). Regional stratigraphy of the south polar layered deposits (Promethei Lingula, Mars): “Discontinuity-bounded” units in images and radargrams. *Icarus*, *308*, 76–107. <https://doi.org/10.1016/j.icarus.2017.08.030>
- Guimpier, A., Conway, S. J., Mangeny, A., Lucas, A., Mangold, N., Peruzzetto, M., et al. (2021). Dynamics of recent landslides (<20 My) on Mars: Insights from high-resolution topography on Earth and Mars and numerical modelling. *Planetary and Space Science*, *206*, 105303. <https://doi.org/10.1016/j.pss.2021.105303>
- Gutiérrez, F., Guerrero, J., & Lucha, P. (2008). A genetic classification of sinkholes illustrated from evaporite paleokarst exposures in Spain. *Environmental Geology*, *53*(5), 993–1006. <https://doi.org/10.1007/s00254-007-0727-5>
- Hare, T. M., Rossi, A. P., Frigeri, A., & Marmo, C. (2018). Interoperability in planetary research for geospatial data analysis. *Planetary and Space Science*, *150*, 36–42. <https://doi.org/10.1016/j.pss.2017.04.004>
- Hargitai, H., & Kereszturi, Á. (2015). *Encyclopedia of planetary landforms*. Springer.
- Haruyama, J., Hioki, K., Shirao, M., Morota, T., Hiesinger, H., van der Bogert, C. H., et al. (2009). Possible lunar lava tube skylight observed by SELENE cameras. *Geophysical Research Letters*, *36*(21), L21206. <https://doi.org/10.1029/2009GL040635>
- He, K., Gkioxari, G., Dollár, P., & Girshick, R. (2018). Mask R-CNN. ArXiv:1703.06870 [Cs]. Retrieved from <http://arxiv.org/abs/1703.06870>
- Hipperson, M., Waldmann, I., Grindrod, P., & Nikolou, N. (2020). Mapping mineralogical distributions on Mars with unsupervised machine learning. *Oral*. <https://doi.org/10.5194/epsc2020-773>
- Hoeser, T., & Kuenzer, C. (2020). Object detection and image segmentation with deep learning on Earth observation data: A review-part I: Evolution and recent trends. *Remote Sensing*, *12*(10), 1667. <https://doi.org/10.3390/rs12101667>
- Hong, I. S., Yi, Y., Yu, J., & Haruyama, J. (2015). 3D modeling of lacus mortis pit crater with presumed interior tube structure. *Journal of Astronomy and Space Sciences*, *32*(2), 113–120. <https://doi.org/10.5140/JASS.2015.32.2.113>
- Hooper, D. M., & Smart, K. J. (2013). Characterization of landslides on Mars and implications for possible failure mechanisms. *Lunar and Planetary Science Conference*, *1719*, 1795.
- Horvath, T., Hayne, P., & Paige, D. (2020). Thermal environments and illumination in lunar pits and lava tubes. *Lunar and Planetary Science Conference*, *2326*, 1729.
- Hu, Y., Xiao, J., Liu, L., Zhang, L., & Wang, Y. (2021). Detection of small impact craters via semantic segmenting lunar point clouds using deep learning network. *Remote Sensing*, *13*(9), 1826. <https://doi.org/10.3390/rs13091826>
- Hungr, O., Leroueil, S., & Picarelli, L. (2014). The Varnes classification of landslide types, an update. *Landslides*, *11*(2), 167–194. <https://doi.org/10.1007/s10346-013-0436-y>
- James, L. A., Harden, C. P., & Clague, J. J. (2013). 13.1 geomorphology of human disturbances, climate change, and hazards. In *Treatise on geomorphology* (pp. 1–13). Elsevier. <https://doi.org/10.1016/B978-0-12-374739-6.00339-0>
- Jiang, F. (2020). Criteria of sinkhole formation in soils from physical models. *Bulletin of Engineering Geology and the Environment*, *79*(7), 3833–3841. <https://doi.org/10.1007/s10064-020-01768-0>
- Kaku, T., Haruyama, J., Miyake, W., Kumamoto, A., Ishiyama, K., Nishibori, T., et al. (2017). Detection of intact lava tubes at Marius Hills on the moon by SELENE (Kaguya) lunar radar sounder: Intact lunar lava tube detection by LRS. *Geophysical Research Letters*, *44*(20), 10155–10161. <https://doi.org/10.1002/2017GL074998>
- Kumar, P., Rawat, J. S., Rehman, S., Sajjad, H., Rani, M., Mohanto, K. K., et al. (2019). Exploring geomorphic Processes and martian Gale crater Topography on Mars using CTX and HiRISE express image dataset (Preprint). *Geosciences—Applied Geology*. <https://doi.org/10.5194/essd-2019-4>
- Lacerda, W., Ehrlich, M., Fontoura, S., & Sayão, A. (2004). Landslides: Evaluation and Stabilization/Glisement de Terrain: Evaluation et Stabilisation, Set of 2 Volumes. In *Proceedings of the Ninth International symposium on landslides, June 28–July 2, 2004*. CRC Press. <https://doi.org/10.1201/b16816>
- Laura, J., Acosta, A., Addair, T., Adoram-Kershner, L., Alexander, J., Alexandrov, O., et al. (2021). Integrated software for imagers and Spectrometers. *Zenodo*. <https://doi.org/10.5281/zenodo.5347823>
- Lee, C. (2019). Automated crater detection on Mars using deep learning. *Planetary and Space Science*, *170*, 16–28. <https://doi.org/10.1016/j.pss.2019.03.008>
- Le Mouélic, S., Enguehard, P., Schmitt, H. H., Caravaca, G., Seignovert, B., Mangold, N., et al. (2020). Investigating lunar boulders at the Apollo 17 landing site using photogrammetry and Virtual reality. *Remote Sensing*, *12*(11), 1900. <https://doi.org/10.3390/rs12111900>
- Léveillé, R. J., & Datta, S. (2010). Lava tubes and basaltic caves as astrobiological targets on Earth and Mars: A review. *Planetary and Space Science*, *58*(4), 592–598. <https://doi.org/10.1016/j.pss.2009.06.004>
- Lin, C.-W., Shieh, C.-L., Yuan, B.-D., Shieh, Y.-C., Liu, S.-H., & Lee, S.-Y. (2004). Impact of Chi-Chi earthquake on the occurrence of landslides and debris flows: Example from the Chenyulan River watershed, Nantou, Taiwan. *Engineering Geology*, *71*(1–2), 49–61. [https://doi.org/10.1016/S0013-7952\(03\)00125-X](https://doi.org/10.1016/S0013-7952(03)00125-X)
- Liu, J. G., Mason, P. J., Clerici, N., Chen, S., Davis, A., Miao, F., et al. (2004). Landslide hazard assessment in the Three Gorges area of the Yangtze River using ASTER imagery: Zigui–Badong. *Geomorphology*, *61*(1–2), 171–187. <https://doi.org/10.1016/j.geomorph.2003.12.004>
- Lohse, V., Heipke, C., & Kirk, R. L. (2006). Derivation of planetary topography using multi-image shape-from-shading. *Planetary and Space Science*, *54*(7), 661–674. <https://doi.org/10.1016/j.pss.2006.03.002>
- Luebke, D. (2008). Cuda: Scalable parallel programming for high-performance scientific computing. 2008 5th IEEE International symposium on biomedical imaging: From Nano to Macro (pp. 836–838). <https://doi.org/10.1109/ISBI.2008.4541126>
- Luzzi, E., Rossi, A. P., Carli, C., & Altieri, F. (2020). Tectono-magmatic, sedimentary, and hydrothermal history of Arsinoes and Pyrrhae Chaos, Mars. *Journal of Geophysical Research: Planets*, *125*(12). <https://doi.org/10.1029/2019JE006341>
- Luzzi, E., Rossi, A. P., Massironi, M., Pozzobon, R., Mestrelli, D., & Corti, G. (2021). Piecemeal Caldera collapse as the trigger of Chaotic terrains and floor-fractured craters on the moon and Mars. In *52nd lunar and planetary science Conference*, 1883.
- Martinot, M., Besse, S., Flahaut, J., Quantin-Nataf, C., Lozac’h, L., & van Westrenen, W. (2018). Mineralogical diversity and geology of Humboldt crater derived using Moon Mineralogy Mapper data. *Journal of Geophysical Research: Planets*, *123*(2), 612–629. <https://doi.org/10.1002/2017je005435>
- Massa, F., & Girshick, R. (2018). maskrcnn-benchmark: Fast, modular reference implementation of instance segmentation and object detection algorithms in PyTorch. Retrieved from <https://github.com/facebookresearch/maskrcnn-benchmark/>
- McEwen, A. S., Eliason, E. M., Bergstrom, J. W., Bridges, N. T., Hansen, C. J., Delamere, W. A., et al. (2007). Mars Reconnaissance orbiter’s high resolution imaging science experiment (HiRISE). *Journal of Geophysical Research*, *112*(E5), E05S02. <https://doi.org/10.1029/2005JE002605>

- Merghadi, A., Yunus, A. P., Dou, J., Whiteley, J., ThaiPham, B., Bui, D. T., et al. (2020). Machine learning methods for landslide susceptibility studies: A comparative overview of algorithm performance. *Earth-Science Reviews*, 207, 103225. <https://doi.org/10.1016/j.earscirev.2020.103225>
- Merkel, D. (2014). Docker: Lightweight linux containers for consistent development and deployment. *Linux Journal*, 2014(239), 2.
- Micheletti, N., Chandler, J. H., & Lane, S. N. (2015). Structure from motion (SfM) Photogrammetry. *Geomorphological Techniques*, 12.
- Michikami, T., Hagermann, A., Miyamoto, H., Miura, S., Haruyama, J., & Lykawka, P. S. (2014). Impact cratering experiments in brittle targets with variable thickness: Implications for deep pit craters on Mars. *Planetary and Space Science*, 96, 71–80. <https://doi.org/10.1016/j.pss.2014.03.010>
- Milkovich, S. M., Plaut, J. J., Safaeinili, A., Picardi, G., Seu, R., & Phillips, R. J. (2009). Stratigraphy of Promethei Lingula, south polar layered deposits, Mars, in radar and imaging data sets. *Journal of Geophysical Research*, 114(E3), E03002. <https://doi.org/10.1029/2008JE003162>
- Miyamoto, H., Uehara, K., Murakawa, M., Sakanashi, H., Nosato, H., Kouyama, T., & Nakamura, R. (2018). Object detection in satellite imagery using 2-step convolutional neural networks. *International Geoscience and Remote Sensing Symposium (IGARSS)*, 2018-July, 1268–1271. <https://doi.org/10.1109/IGARSS.2018.8518587>
- Muller, J.-P., Tao, Y., Putri, A. R. D., & Conway, S. J. (2021). 3D multi-resolution mapping of MARS using CASP-GO ON HRSC, CRISM, CTX and HIRISE. *The International Archives of the Photogrammetry, Remote Sensing and Spatial Information Sciences*, XLIII-B3-2021, 667–671. <https://doi.org/10.5194/isprs-archives-XLIII-B3-2021-667-2021>
- Nagle-McNaughton, T., McClanahan, T., & Scuderi, L. (2020). PlanNet: A neural network for detecting Transverse aeolian ridges on Mars. *Remote Sensing*, 12(21), 3607. <https://doi.org/10.3390/rs12213607>
- Napierski, J., Barr, I., Kamp, U., & Kervyn, M. (2013). 3.8 remote sensing and GIScience in geomorphological mapping. In *Treatise on geomorphology* (pp. 187–227). Elsevier. <https://doi.org/10.1016/B978-0-12-374739-6.00050-6>
- NASA. (2021). Nasa BRAILLE—biologic and resource analog Investigations in low light environments. Retrieved from <https://nasa-braille.org/>
- Naß, A., Di, K., Elgner, S., van Gasselt, S., Hare, T., Hargitai, H., et al. (2017). Planetary cartography and mapping: Where we are today, and where we are heading for? *The International Archives of the Photogrammetry, Remote Sensing and Spatial Information Sciences*, XLII-3, 105–112. <https://doi.org/10.5194/isprs-archives-XLII-3-W1-105-2017>
- Naß, A., Massironi, M., Rossi, A., Penasa, L., Pozzobon, R., Brandt, C., et al. (2021). Streamlining European mapping efforts: The geologic mapping of planetary bodies (GMAP) (p. 7034, Vol. 2610). Retrieved from <https://elib.dlr.de/142475/>
- Naß, A., & van Gasselt, S. (2021). The geologic map of the Cassini quadrangle on the Moon: Planetary cartography between science, efficacy and cartographic aesthetics. *International Journal of Cartography*, 7(2), 178–183. <https://doi.org/10.1080/23729333.2021.1912886>
- Nass, A., van Gasselt, S., Hare, T., & Hargitai, H. (2021). 50 Years of sensor-based planetary cartography: Review and perspectives. *Proceedings of the ICA*, 4, 1–8. <https://doi.org/10.5194/ica-proc-4-76-2021>
- Nodjoumi, G. (2021a). DeepLandforms: A deep learning computer vision toolset applied to a prime use case for mapping planetary skylights—ANc [Dataset]. stl. <https://doi.org/10.5281/zenodo.7351391>
- Nodjoumi, G. (2021b). *ImageProcessingUtils: Docker container, Jupyter Notebook and CLI*. <https://doi.org/10.5281/zenodo.6247608>
- Nodjoumi, G. (2021c). *DeepLandforms*. First Release. <https://doi.org/10.5281/zenodo.7488867>
- Nodjoumi, G., Brandt, C., & Rossi, A. P. (2022). Open-source planetary data processing environments based on JupyterHub and Docker containers (Vol. 2).
- Nodjoumi, G., Pozzobon, R., & Rossi, A. P. (2021). Deep learning object detection for mapping cave candidates on MARS: Building UP the MARS global cave candidate catalog (MGC<sup>3</sup>). *Lunar and Planetary Science Conference*, 2548. <https://www.hou.usra.edu/meetings/lpsc2021/pdf/1316.pdf>
- Open Geospatial Consortium. (2021). OGC® GeoPackage encoding standard. Retrieved from <https://www.geopackage.org/spec/>
- Palafox, L. F., Hamilton, C. W., Scheidt, S. P., & Alvarez, A. M. (2017). Automated detection of geological landforms on Mars using Convolutional Neural Networks. *Computers & Geosciences*, 101, 48–56. <https://doi.org/10.1016/j.cageo.2016.12.015>
- Parente, M., Itoh, Y., & Saranathan, A. (2019). New CRISM data products for improved characterization and analysis of the Mars2020 landing site. *IGARSS 2019—2019 IEEE International Geoscience and Remote Sensing Symposium*, 4911–4914. <https://doi.org/10.1109/IGARSS.2019.8899313>
- Parise, M. (2019). Sinkholes. In *Encyclopedia of caves* (pp. 934–942). Elsevier. <https://doi.org/10.1016/B978-0-12-814124-3.00110-2>
- Paul, S., & Ganju, S. (2021). Flood segmentation on sentinel-1 SAR imagery with semi-supervised learning. ArXiv:2107.08369 [Cs]. Retrieved from <http://arxiv.org/abs/2107.08369>
- PDS Geosciences Nodes. (2021). Orbital data explorer—Mars holdings. Retrieved from [https://ode.rsl.wustl.edu/odeholdings/Mars\\_holdings.html](https://ode.rsl.wustl.edu/odeholdings/Mars_holdings.html)
- Pham, M.-T., Courtrai, L., Friguet, C., Lefèvre, S., & Baussard, A. (2020). YOLO-Fine: One-Stage detector of small objects under various backgrounds in remote sensing images. *Remote Sensing*, 12(15), 2501. <https://doi.org/10.3390/rs12152501>
- Pipán, T., & Culver, D. C. (2019). Chapter 107—Shallow subterranean habitats. In W. B. White, D. C. Culver, & T. Pipán (Eds.), *Encyclopedia of caves* (3rd ed., pp. 896–908). Academic Press. <https://doi.org/10.1016/B978-0-12-814124-3.00107-2>
- Pondrelli, M., Frigeri, A., Marinangeli, L., Di Pietro, I., Pantaloni, M., Pozzobon, R., et al. (2020). Geological and geomorphological mapping of Martian sedimentary deposits: An attempt to identify current practices in mapping and representation. *Oral*. <https://doi.org/10.5194/eps2020-232>
- Rashno, A., Nazari, B., Sadri, S., & Saraei, M. (2017). Effective pixel classification of Mars images based on ant colony optimization feature selection and extreme learning machine. *Neurocomputing*, 226, 66–79. <https://doi.org/10.1016/j.neucom.2016.11.030>
- Redmon, J., Divvala, S., Girshick, R., & Farhadi, A. (2016). You only look once: Unified, real-time object detection. *Proceedings—IEEE Computer Society Conference on Computer Vision and Pattern Recognition*. <https://doi.org/10.1109/CVPR.2016.91>
- Robbins, S. J., & Hynes, B. M. (2014). The secondary crater population of Mars. *Earth and Planetary Science Letters*, 400(2012), 66–76. <https://doi.org/10.1016/j.epsl.2014.05.005>
- Robinson, M. S., Brylow, S. M., Tschimmel, M., Humm, D., Lawrence, S. J., Thomas, P. C., et al. (2010). Lunar reconnaissance orbiter Camera (LROC) instrument overview. *Space Science Reviews*, 150(1–4), 81–124. <https://doi.org/10.1007/s11214-010-9634-2>
- Rousset, G., Despinoy, M., Schindler, K., & Mangeas, M. (2021). Assessment of deep learning techniques for land use land cover classification in southern New Caledonia. *Remote Sensing*, 13(12), 2257. <https://doi.org/10.3390/rs13122257>
- Salese, F., Pondrelli, M., Neeseman, A., Schmidt, G., & Ori, G. G. (2019). Geological evidence of planet-wide groundwater system on Mars. *Journal of Geophysical Research: Planets*, 124(2), 374–395. <https://doi.org/10.1029/2018JE005802>
- Sargeant, H. M., Bickel, V. T., Honniball, C. I., Martinez, S. N., Rogaski, A., Bell, S. K., et al. (2020). Using boulder tracks as a tool to understand the Bearing capacity of permanently shadowed regions of the moon. *Journal of Geophysical Research: Planets*, 125(2). <https://doi.org/10.1029/2019JE006157>



- Sauro, F., Pozzobon, R., Massironi, M., De Berardinis, P., Santagata, T., & De Waele, J. (2020). Lava tubes on Earth, moon and Mars: A review on their size and morphology revealed by comparative planetology. *Earth-Science Reviews*, 209, 103288. <https://doi.org/10.1016/j.earscirev.2020.103288>
- Sauro, U. (2016). Dolines and sinkholes: Aspects of evolution and problems of classification. *Acta Carsologica*, 32(2). <https://doi.org/10.3986/ac.v32i2.335>
- Servis, K., Lagain, A., Benedix, G., Flannery, D., Norman, C., Towner, M., & Paxman, J. (2020). Automatic crater detection over the Jezero crater area from HiRISE imagery. *pico*. <https://doi.org/10.5194/egusphere-egu2020-6269>
- Sharma, R., & Srivastava, N. (2021). Detection and classification of skylights on the flank of Elysium Mons, Mars (Preprint). *Geology*. <https://doi.org/10.1002/essoar.10506123.1>
- Silburt, A. (2019). DeepMoon—lunar crater counting through deep learning. [Python](Original work published 2017). Retrieved from <https://github.com/silburt/DeepMoon>
- Silburt, A., Ali-Dib, M., Zhu, C., Jackson, A., Valencia, D., Kissin, Y., et al. (2019). Lunar Crater identification via deep learning. *Icarus*, 317, 27–38. <https://doi.org/10.1016/j.icarus.2018.06.022>
- Sivakumar, V., Neelakantan, R., & Santosh, M. (2017). Lunar surface mineralogy using hyperspectral data: Implications for primordial crust in the Earth–Moon system. *Geoscience Frontiers*, 8(3), 457–465. <https://doi.org/10.1016/j.gsf.2016.03.005>
- Skjetne, H. L., Singer, K. N., Hynek, B. M., Knight, K. I., Schenk, P. M., Olkin, C. B., et al. (2021). Morphological comparison of blocks in chaos terrains on Pluto, Europa, and Mars. *Icarus*, 356, 113866. <https://doi.org/10.1016/j.icarus.2020.113866>
- Slymaker, O., Spencer, T., & Embleton-Hamann, C. (2021). Recasting geomorphology as a landscape science. *Geomorphology*, 384, 107723. <https://doi.org/10.1016/j.geomorph.2021.107723>
- Smith, Z., Tullis, J., Steele, K., & Malfavon, L. (2006). Martian sinkholes: Implications for large scale evaporite deposits. *37th Annual Lunar and Planetary Science Conference*, 1071.
- Stepinski, T. F., Ghosh, S., & Vilalta, R. (2007). Machine learning for automatic mapping of planetary surfaces. <https://doi.org/10.13140/2.1.1518.9445>
- Su, S., Fanara, L., Zhang, X., Gwinner, K., Hauber, E., & Oberst, J. (2021). Detecting the sources of ice block falls at the martian north polar scarps by analysis of multi-temporal HiRISE imagery. *The International Archives of the Photogrammetry, Remote Sensing and Spatial Information Sciences, XLIII-B3-2021*, 673–678. <https://doi.org/10.5194/isprs-archives-XLIII-B3-2021-673-2021>
- Sun, V. Z., & Stack, K. M. (2020). Geologic map of Jezero crater and the Nili Planum region, Mars. In *Geologic map of Jezero crater and the Nili Planum region, Mars (USGS numbered series No. 3464; Scientific Investigations Map)* (Vol. 3464). U.S. Geological Survey. <https://doi.org/10.3133/sim3464>
- Szegedy, C., Toshev, A., & Erhan, D. (2013). Deep neural networks for object detection. *Advances in Neural Information Processing Systems*, 26(NIPS). <https://doi.org/10.1109/CVPR.2014.276.2013>
- Talukdar, S., Singha, P., Mahato, S., Pal, S., Liou, Y.-A., Rahman, A., & Rahman, A. (2020). Land-use land-cover classification by machine learning classifiers for satellite observations—A review. *Remote Sensing*, 12(7), 1135. <https://doi.org/10.3390/rs12071135>
- Tempfli, K., Huurneman, G. C., Bakker, W. H., Janssen, L. L. F., Feringa, W. F., Gieske, A. S. M., et al. (2009). *Principles of remote sensing: An introductory textbook*. ITC.
- Tien Bui, D., Tuan, T. A., Klempe, H., Pradhan, B., & Revhaug, I. (2016). Spatial prediction models for shallow landslide hazards: A comparative assessment of the efficacy of support vector machines, artificial neural networks, kernel logistic regression, and logistic model tree. *Landslides*, 13(2), 361–378. <https://doi.org/10.1007/s10346-015-0557-6>
- Tirsch, D., Voigt, J. R. C., Viviano, C. E., Bishop, J. L., Lane, M. D., Tornabene, L. L., & Loizeau, D. (2021). *Spatial trends in mineral Abundances across Tyrrhena Terra on Mars derived from geomorphological and Mineralogical mapping*. EGU General Assembly Conference Abstracts. EGU21-7440.
- Tsibulskaya, V., Hepburn, A. J., Hubbard, B., & Holt, T. (2020). Surficial geology and geomorphology of Greg crater, Promethei Terra, Mars. *Journal of Maps*, 16(2), 524–533. <https://doi.org/10.1080/17445647.2020.1785343>
- Ultralytics/yolov5. (2021). [Python]. Ultralytics. (Original work published 2020). Retrieved from <https://github.com/ultralytics/yolov5>
- Van Den Eeckhaut, M., Poesen, J., Govers, G., Verstraeten, G., & Demoulin, A. (2007). Characteristics of the size distribution of recent and historical landslides in a populated hilly region. *Earth and Planetary Science Letters*, 256(3–4), 588–603. <https://doi.org/10.1016/j.epsl.2007.01.040>
- van der Bogert, C. H., & Ashley, J. W. (2015). Skylight. In H. Hargitai & Á. Kereszturi (Eds.), *Encyclopedia of planetary landforms* (pp. 1–7). Springer. [https://doi.org/10.1007/978-1-4614-9213-9\\_342-2](https://doi.org/10.1007/978-1-4614-9213-9_342-2)
- Wada, K. (2021). Labelme: Image Polygonal annotation with Python. <https://doi.org/10.5281/zenodo.5711226>
- Wagner, R. V., & Robinson, M. S. (2014). Distribution, formation mechanisms, and significance of lunar pits. *Icarus*, 237, 52–60. <https://doi.org/10.1016/j.icarus.2014.04.002>
- Wang, S., Fan, Z., Li, Z., Zhang, H., & Wei, C. (2020). An effective lunar crater recognition algorithm based on convolutional neural network. *Remote Sensing*, 12(17), 2694. <https://doi.org/10.3390/rs12172694>
- Wang, Y., Wu, B., Xue, H., Li, X., & Ma, J. (2021). An improved global catalog of lunar impact craters ( $\geq 1$  km) with 3D morphometric information and updates on global crater analysis. *Journal of Geophysical Research: Planets*, 126(9), e2020JE006728. <https://doi.org/10.1029/2020je006728>
- Watkins, R., Jolliff, B., Lawrence, S., Hayne, P., & Ghent, R. (2017). Boulder distributions at legacy landing sites: Assessing regolith production rates and landing site hazards.
- Watters, W. A., Geiger, L. M., Fendrock, M., & Gibson, R. (2015). Morphometry of small recent impact craters on Mars: Size and terrain dependence, short-term modification. *Journal of Geophysical Research: Planets*, 120(2), 226–254. <https://doi.org/10.1002/2014je004630>
- Whitten, J. L., & Martin, E. S. (2019). Icelandic pit chains as planetary analogs: Using morphologic measurements of pit chains to determine Regolith thickness. *Journal of Geophysical Research: Planets*, 124(11), 2983–2999. <https://doi.org/10.1029/2019JE006099>
- Wilhelm, T., Geis, M., Pütschneider, J., Sievernich, T., Weber, T., Wohlfarth, K., & Wöhler, C. (2020). DoMars16k: A diverse dataset for weakly supervised geomorphologic analysis on Mars. *Remote Sensing*, 12(23), 3981. <https://doi.org/10.3390/rs12233981>
- Wu, B., Li, F., Hu, H., Zhao, Y., Wang, Y., Xiao, P., et al. (2020). Topographic and geomorphological mapping and analysis of the Chang'E-4 landing site on the far side of the moon. *Photogrammetric Engineering & Remote Sensing*, 86(4), 247–258. <https://doi.org/10.14358/pers.86.4.247>
- Wu, Y., Kirillov, A., Massa, F., Lo, W.-Y., & Girshick, R. (2019a). Detectron2 is FAIR's next-generation platform for object detection, segmentation and other visual recognition tasks. <https://github.com/facebookresearch/detectron2>
- Wu, Y., Kirillov, A., Massa, F., Lo, W.-Y., & Girshick, R. (2019b). Detectron2/MODEL\_ZOO.md at main facebookresearch/detectron2 [https://github.com/facebookresearch/detectron2/blob/main/MODEL\\_ZOO.md](https://github.com/facebookresearch/detectron2/blob/main/MODEL_ZOO.md)
- Wu, Y., Kirillov, A., Massa, F., Lo, W.-Y., Girshick, R., & Facebook, Inc. (2020). facebookresearch/detectron2: Detectron2 is FAIR's next-generation platform for object detection and segmentation. Retrieved from <https://github.com/facebookresearch/detectron2>



- Wyrick, D. (2004). Distribution, morphology, and origins of Martian pit crater chains. *Journal of Geophysical Research*, *109*(E6), E06005. <https://doi.org/10.1029/2004JE002240>
- Xiao, Z., Zeng, Z., & Komatsu, G. (2014). A global inventory of central pit craters on the Moon: Distribution, morphology, and geometry. *Icarus*, *227*, 195–201. <https://doi.org/10.1016/j.icarus.2013.09.019>
- Yousefi, S., Pourghasemi, H. R., Emami, S. N., Pouyan, S., Eskandari, S., & Tiefenbacher, J. P. (2020). A machine learning framework for multi-hazards modeling and mapping in a mountainous area. *Scientific Reports*, *10*(1), 12144. <https://doi.org/10.1038/s41598-020-69233-2>
- Youssef, A. M., El-Kaliouby, H., & Zabramawi, Y. A. (2012). Sinkhole detection using electrical resistivity tomography in Saudi Arabia. *Journal of Geophysics and Engineering*, *9*(6), 655–663. <https://doi.org/10.1088/1742-2132/9/6/655>
- Zhang, A., Lipton, Z. C., Li, M., & Smola, A. J. (2021). 4.4.3 underfitting or overfitting? In *Dive into deep learning* (pp. 146–147). Retrieved from <http://arxiv.org/abs/2106.11342>
- Zhao, Z. Q., Zheng, P., Xu, S. T., & Wu, X. (2019). Object detection with deep learning: A review. *IEEE Transactions on Neural Networks and Learning Systems*, *30*(11), 3212–3232. <https://doi.org/10.1109/TNNLS.2018.2876865>